Weighted Average Continuity Approach and Moment Correction New strategies for non-consistent mesh projection in structural mechanics

Simone Coniglio, Christian Gogu, Joseph Morlier

Archives of Computational Methods in Engineering manuscript No.
(will be inserted by the editor)

Weighted Average Continuity Approach and Moment Correction

New strategies for non-consistent mesh projection in structural mechanics

Simone Coniglio · Christian Gogu · Joseph Morlier

Received: date / Accepted: date

Abstract Tying non-matching meshes is needed in many instances of finite element modeling. Multiple techniques have been proposed in the literature to accomplish the correct communication between different discretizations. They all seek to achieve some trade-off in terms of accuracy, complexity and computational cost. In this work we review several of the existing techniques and benchmark them on several simple test problems in terms of accuracy and computational cost. We also discuss some of the drawbacks and limitations of the existing methods. We then propose two novel contributions. First, a new approach that imposes the continuity of the displacement field at the interface in a point-wise manner only after an integral weighted averaging procedure over each interface. Second, a procedure for the correction of the interpolation operator based on the balance of internal forces and moments at the interface is proposed, which is applicable to all the reviewed methods, both existing and the new proposed one. All the considered approaches are benchmarked on several test problems in terms of various error measures for displacements, stresses, interface forces and moments, total work at the interface and computational cost.

Keywords Non-matching grids · FEM · mesh projection

1 Introduction

Finite Element Modelling (FEM) is the most popular approximation method used to solve Partial Derivatives Equation (PDE) problems in industrial applications. FEM provides me-

Simone Coniglio · Joseph Morlier
Institut Clément Ader (ICA),Université de Toulouse , CNRS, ISAE-SUPAERO, UPS, INSA, Mines-Albi,
3 rue Caroline Aigle, 31400 Toulouse, France

Christian Gogu
Institut Clément Ader (ICA),Université de Toulouse , CNRS, UPS, INSA, ISAE-SUPAERO, Mines-Albi,
3 rue Caroline Aigle, 31400 Toulouse, France
Corresponding author:
E-mail: christian.gogu@gmail.com

Simone Coniglio
Airbus Operations S.A.S.
316 route de Bayonne 31060 Toulouse Cedex 09 France

chanical responses of solid structures under prescribed load and Boundary Conditions (BCs). This can be useful for the design and validation phase, to avoid costly full scale testing and to improve the overall design process. Situations arise where a finite element model needs to be assembled from parts that can present non-matching grids (meshes) and elemental formulation. In these cases the displacement at the interface is not unequivocally determined and special techniques have to be used to take into account the non-conforming interface [56]. This can be the case:

- When two parts have to be meshed independently for practical reasons [4, 62]. This can be due to the impossibility to get good quality meshes for two adjacent components or due to models being generated independently by different teams or for different purposes, or even for modularity if one component model has to be integrated in different product models.
- When different physical phenomena are studied with different discretizations: for example in acoustics [39]. One of the most popular application is Fluid-Structure Interaction (FSI) [6, 12, 16, 23, 35, 46, 54]. The mesh needed for the fluid is much finer than the one that can be used for solid. Important computation time can be saved using mesh projection techniques to connect different meshes.
- When the domain decomposition is required ([13, 34, 36, 37, 55]. The communication between the large scale and lower scale meshes is often done with mesh projection operator. Such domain decomposition is for example useful when a much finer mesh is needed in a localized region of a structure (e.g. in crack propagation analysis [34, 52, 53]).
- When contact between meshes is activated in the simulation [20, 65, 67, 75]. In the most general situation rebounding and sliding can appear the exchange of information between meshes changes with the grid configurations. In this application the mesh projection operator have to be computed fast enough so that their evaluation can be repeated in the analysis.

This paper choses to mainly focus on the first point mentioned, but the final conclusions may be applicable to several of the other cases as well. The main challenge of the aforementioned situation is to ensure the continuity of the displacement field at the non-conforming interface. In the general case of non-matching interfaces, the displacement field will be continuous at the cost of an over-constraint of the interface [63]. To avoid this phenomenon, typically both strong and weak coupling can be employed to satisfy the compatibility of the solution at the interface node DOFs. The strong coupling techniques are also referred to as collocation techniques [1, 63] or node to segment [75] methods, as one constraint equation is assigned to each interface node DOF. In the weak coupling also called segment to segment [75] methods, on the other hand, the continuity is written in an integral or averaged sense. To avoid interface stiffening, the weak formulation is preferred [1, 38]. For both these "classic" approaches, one surface is chosen to be the one that will produce the constraint equations (slave surface) and the other is considered as interpolating (master surface). Each DOF of the slave surface is then written as a linear combination of the DOFs of the master surface. Once that this linear system of constraint equation is written, the final displacement solution can be obtained by the elimination method [4] i.e. substituting the slave node DOFs variable with their expression in terms of master node DOFs. Since the solution of a static solid analysis can also be considered as a minimization problem, the linear constraints can be imposed using the Lagrange multipliers approach [2, 9]. A variable is therefore created for each constraint that has to be satisfied and used to build the Lagrangian function. The stationary conditions of the Lagrangian function give the linear system of equation used to find

the nodal displacement and the interface Lagrange multiplier variables. The latter also have the physical interpretation of interface internal forces. One of the most used techniques that utilizes Lagrange multipliers in a continuous form is the Mortar approach [7, 8, 60, 61].The distribution functions for the Lagrange multipliers and shape functions for the finite elements should be properly selected to fulfill the Ladyzhenskaya-Babuška-Brezzi (LBB) condition (also known as the inf-sup condition) [3] in order to guarantee that both discretizations converge to the correct solution with the mesh refinement. Other numerical schemes followed, inspired by the optimization community. In the PhD dissertation of Rixen [63] one can find a method based on the augmented Lagragian method in optimization. In the review of Barlow [4] another method based on the external penalty approach is presented. The main difficulty of this approach consists in the choice of the penalty factor. Deparis et al. introduced in [26] a new approach based on the simultaneous continuity of the displacement and the internal loads per unit of area at the interface. This promising techniques has been tested in the case of a simple patch test and more complex fluid structure interaction problems. In those cases the method reveals the same performance as Mortar, with a much smaller computational effort and programming complexity. In order to pass *a priori* the simple stress patch test even for curved interfaces where Mortar typically fails, Park et al [59] developed a method based on the introduction of a third displacement field whose nodes are placed based on an equilibrium equation of moments. The resulting scheme is however quite complex and the applications considered in [59] where only for a simple 2D case and a planar interface on a 3D case. For overlapped domains with non consistent domains the Arlerquin method has also been proposed [28, 29]. More invasive approaches were developed by Cho et al. [17–19],Lim et al. [49, 50] , Kim et al. [48] and Duarte [32], where the idea is to modify the Element shape functions adding some nodes to the element of the interface or enriching the shape functions. In Dohrman et al. [30,31] the slave element locations and formulations are modified in order to transform a non-conforming interface into a conforming one. In Tian et al. [72] interface elements formulation is replaced with a meshless formulation. In this way the coupled analysis becomes straightforward but the implementation of a special formulation for interface elements is not as simple as the application of multipoint constraints (MPCs) at the interface. A Least Square Method can be found in Bochev et al. [11] in order to pass a simple patch test. This method requires nevertheless the meshes to be perturbed at the interface to avoid gaps between curved interface, which renders the approach more complex to implement. Bitencourt et al. [10] introduced a new method that assembles Coupling Finite Elements (CFEs) at the interface to build the constraints equation between interfaces Degrees of Freedom (DOFs). This approach was studied for 3D planar, 2D planar or 2D curved interfaces. A recent method was developed by Cafiero et al. [15] on the base of the previous developments of Nitsche [57], Becker [5], Heintz [44] , Olivier [58] and Hartman [43]. This approach, inspired from the contact community avoids the expensive segment to segment projections needed for the mortar approach introducing a particular formulation in the gap between the non conforming meshes at the interface.The DIM approach [15] was also extended to the case of mixed fields as can be encoutered in multiphysics problems [51]. Another similar approach introduced virtual gap elements at the interface of the domains and imposes a zero strain condition to these elements [68].
In this article we first review and analyze several of the existing approaches for tying non conforming interfaces. After describing their formulation and implementation we discuss their advantages and drawbacks. All the considered approaches are then benchmarked on several simple test problems in terms of accuracy, computational cost and implementation complexity. We then propose two novel contributions. First, a new approach is proposed that imposes the continuity of the displacement field at the interface in a point-wise manner only

after an integral weighted averaging procedure over each interface. This approaches seeks to improve the accuracy of the stresses, while maintaining relatively low computational cost and implmentation complexity. Second, a procedure is proposed for the correction of the interpolation operator based on the balance of internal forces and moments at the interface. This approach is applicable to all the reviewed approaches and aims to improve their accuracy.

The rest of this article is structured as follows. In section 2 We introduce notations related to the governing equations for solid elasto-statics and the finite element discretization. In section 3 the basic equations of the elimination approach are obtained, and the conservation of energy and sum of residual at the interface is transposed in terms of requirements on the interpolation operator. Then several existing mesh tying techniques are introduced, among the strong coupling The Radial Basis Function (RBF) [6], [66] and Element Shape Function (ESF) [1] interpolations, are presented in details. As an example of weak coupling we present in section 3.1.3 the Weighted Residual Method (WRM) whose displacement solution is the same as of the Mortar approach and of the continuous least squares approach presented in [63]. The implementation we propose here is quite different from the one originally presented by Puso [60,61] as will be descibed in subsection 3.1.3. In subsection 3.2 the variational principle and the Mortar formulation with Lagrange multipliers are summarized. The internodes [26] formulation is presented in subsection 3.3, starting from the physical hypothesis behind this method giving its matrix formulation. The simplicity of the internodes formulation inspired us to develop a new approach we call Weighted Average Continuity Approach (WACA), which seeks to maintain low implementation complexity and computational cost, similar to the Internodes apporach, but achieve improved stress accuracy, similar to the Mortar approach. The idea of the proposed WACA method is to make a RBF/ESF interpolation, not directly of the displacement field but of its weighted integral average on each interface (master and slave). This leads to a simple and conservative approach that improves the accuracy of the RBF interpolation. A second novel contribution presented in subsection 3.5 consists in the *a priori* balance of the total moment and force residuals that defines six constraints per each line of the projection operator. These are used to produce a vector subspace on which one can project the interpolation operator line obtained from an elimination method to get a new interpolation operator, which significantly improves accuracy. In section 4 a numerical test battery is presented for benchmarking the performance of RBF interpolation, WRM, WACA and internodes method. The methods are compared in section 4.2 in terms of several metrics, including accuracy of the displacements, stresses, interface forces and moments, total work at the interface. The conclusion of this study are finally outlined in section 5.

2 Continuous elastostatics problem for partitioned domains and consistent finite element discretization

The main goal of section 2 is to introduces notations associated with the finite element formulations for the problem at hand, notations which will be used throughout the rest of the article.

[1] In this paper we call ESF the use of element shape function to interpolate the displacement field at the interface.

2.1 Elastostatics equations - strong and weak form

We consider an elastic body described by a 3D domain Ω (cf. figure 1). We denote its boundary $\partial\Omega$ and the outward normal vector $\hat{\boldsymbol{n}}$. Finally we call $\partial\Omega_u$ and $\partial\Omega_\sigma$ the boundary where respectively displacements and surface traction are prescribed, so that $\partial\Omega_\sigma \cup \partial\Omega_u = \partial\Omega$.

In elastostatic problems one seeks the displacement field $\boldsymbol{u}(\boldsymbol{x}) \in H^1(\Omega)$ that solves the

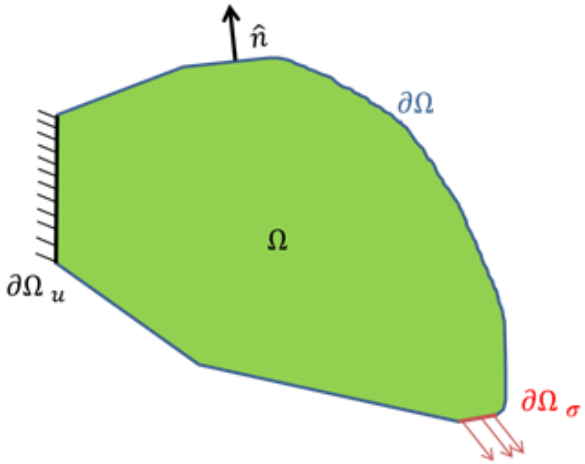

Fig. 1: linear elastostatics problem definition

local balance, boundary conditions and constitutive equations:

$$\nabla \cdot \boldsymbol{\sigma} + \boldsymbol{b} = \boldsymbol{0} \quad \forall \boldsymbol{x} \in \Omega / \partial\Omega \tag{1}$$
$$\boldsymbol{u} = \bar{\boldsymbol{u}} \quad \forall \boldsymbol{x} \in \partial\Omega_u \tag{2}$$
$$\boldsymbol{\sigma} \cdot \hat{\boldsymbol{n}} = \bar{\boldsymbol{t}} \quad \forall \boldsymbol{x} \in \partial\Omega_\sigma \tag{3}$$
$$\boldsymbol{\sigma} = \boldsymbol{E} : \varepsilon \quad \forall \boldsymbol{x} \in \Omega \tag{4}$$

Where $\boldsymbol{b}$ are the body force vector, $\boldsymbol{\sigma}$ is the stress tensor and $\nabla \cdot (\bullet)$ indicate the divergence operator, $\bar{\boldsymbol{u}}(\boldsymbol{x})$ and $\bar{\boldsymbol{t}}(\boldsymbol{x})$ are respectively the prescribed displacements field and surface force field defined on the boundary $\partial\Omega_\sigma$ and $\partial\Omega_u$, $\boldsymbol{E}$ is the fourth order elastic tensor and $\varepsilon(\boldsymbol{u}(\boldsymbol{x})) = \boldsymbol{D} \cdot \boldsymbol{u}$ is the infinitesimal strain tensor ($\boldsymbol{D}$ denotes the symmetric gradient operator). In order to use a finite element approach to discretize the elastostatics equations, a weak form of equation (1) is introduced. By evaluating the scalar product of equation (1) with a compatible virtual displacement $\boldsymbol{v}(\boldsymbol{x}) \in \mathbb{V}$ and integrating it over the domain Ω, the weak or integral formulation is obtained:

$$\int_{\partial\Omega_\sigma} (\boldsymbol{v} \cdot \bar{\boldsymbol{t}}) d\partial\Omega + \int_\Omega (\boldsymbol{v} \cdot \boldsymbol{b}) d\Omega = \int_\Omega (\boldsymbol{D} \cdot \boldsymbol{v} : \boldsymbol{E} : \boldsymbol{D} \cdot \boldsymbol{u}) d\Omega \tag{5}$$

2.2 Domain partition

We consider here the same problem but this time we consider a partition of the domain Ω into two subdomains Ω_1 and Ω_2 (cf. figure 2). The general case with m subdomain can be easily derived by this case. The surface used for the partition is unique ($\Gamma_1 \equiv \Gamma_2 \equiv \Gamma$), as a consequence:

$$\boldsymbol{u}_{\Gamma_1} = \boldsymbol{u}_{\Gamma_2} \ \forall \boldsymbol{x} \in \Gamma \tag{6}$$

$$\boldsymbol{E} : \boldsymbol{D}\boldsymbol{u}_{\Gamma_1} \cdot \hat{\boldsymbol{n}}_{\Gamma_1} = \boldsymbol{t}_{12} = -\boldsymbol{t}_{21} = -\boldsymbol{E} : \boldsymbol{D}\boldsymbol{u}_{\Gamma_2} \cdot \hat{\boldsymbol{n}}_{\Gamma_2} \ \forall \boldsymbol{x} \in \Gamma \tag{7}$$

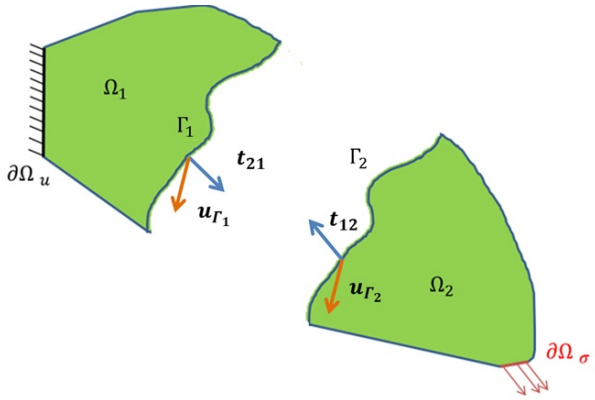

Fig. 2: Partition of Ω in two subdomains Ω_1, Ω_2

Moreover taking in account the partition we will have:[2]

$$\int_{\Gamma_1} (\boldsymbol{v} \cdot \boldsymbol{t}_{21}) d\Gamma_1 + \int_{\partial\Omega_{\sigma_1}} (\boldsymbol{v} \cdot \bar{\boldsymbol{t}}) d\partial\Omega + \int_{\Omega_1} (\boldsymbol{v} \cdot \boldsymbol{b}) d\Omega = \int_{\Omega_1} (\boldsymbol{D}\boldsymbol{v} : \boldsymbol{E} : \boldsymbol{D}\boldsymbol{u}) d\Omega \tag{8}$$

$$\int_{\Gamma_2} (\boldsymbol{v} \cdot \boldsymbol{t}_{12}) d\Gamma_2 + \int_{\partial\Omega_{\sigma_2}} (\boldsymbol{v} \cdot \bar{\boldsymbol{t}}) d\partial\Omega + \int_{\Omega_2} (\boldsymbol{v} \cdot \boldsymbol{b}) d\Omega = \int_{\Omega_2} (\boldsymbol{D}\boldsymbol{v} : \boldsymbol{E} : \boldsymbol{D}\boldsymbol{u}) d\Omega \tag{9}$$

That may be combined with equation (7) to get equation (5). As expected the virtual partition into subdomain is a choice that do not affect the solution of the elastostatics problem.

2.3 Popular discretization using Finite Element

In the standard Galerkin formulation of the finite element method the space of the solution $\mathbb{U}$ and the space of test functions $\mathbb{V}$ are approximated by their discrete approximation: $\mathbb{U}^h$

[2] In these expression the terms $\int_{\Gamma_1} (\boldsymbol{v} \cdot \boldsymbol{t}_{21}) d\Gamma_1$ and $\int_{\Gamma_2} (\boldsymbol{v} \cdot \boldsymbol{t}_{12}) d\Gamma_2$ is due to the work of internal forces at the boundary in a variational approach it would naturally vanishes considering the work over the whole structure.

and $\mathbb{V}^h$ that are given by the linear combination of shape functions defined in each element[3]. so that the test function and the displacement field can be approximated as follows:

$$\boldsymbol{v}(\boldsymbol{x}) = \boldsymbol{N}^{(h)}(\boldsymbol{x})\boldsymbol{v}^{(h)} \qquad \boldsymbol{u}(\boldsymbol{x}) = \boldsymbol{N}^{(h)}(\boldsymbol{x})\boldsymbol{u}^{(h)} \tag{10}$$

In which $\boldsymbol{v}^{(h)}$ and $\boldsymbol{u}^{(h)}$ are the vectors containing the corresponding field values at each node for each degree of freedom, $\boldsymbol{N}^{(h)}(\boldsymbol{x})$ is the $N_d \times N_d N$ matrix, N_d is the number of DOFs per node, N is the number of nodes of the discretization. Accordingly in a 3-D mesh with solid elements $\boldsymbol{N}^{(h)}(\boldsymbol{x})$ has the following structure:

$$\boldsymbol{N}^{(h)}(\boldsymbol{x}) = \begin{bmatrix} N_1(\boldsymbol{x})\boldsymbol{I}_d & N_2(\boldsymbol{x})\boldsymbol{I}_d & \cdots & N_j(\boldsymbol{x})\boldsymbol{I}_d & \cdots & N_N(\boldsymbol{x})\boldsymbol{I}_d \end{bmatrix} \tag{11}$$

Where $\boldsymbol{I}_d$ is the $N_d \times N_d$ identity matrix. Using the discretization of equation (10), the problem of equation (5) can be written as the well known system of equation:

$$\boldsymbol{K}^{(h)}\boldsymbol{u}^{(h)} = \boldsymbol{f}^{(h)} \tag{12}$$

Typically $\boldsymbol{K}^{(h)}$ and $\boldsymbol{f}^{(h)}$ are called *stiffness matrix* and *load vector*. They are defined as:

$$K_{i,j}^{(h)} = \int_{\Omega} (\boldsymbol{D}\cdot\boldsymbol{N}_i^{(h)}(\boldsymbol{x}) : \boldsymbol{E} : \boldsymbol{D}\cdot\boldsymbol{N}_j^{(h)}(\boldsymbol{x}))d\Omega \tag{13}$$

$$f_i^{(h)} = \int_{\partial\Omega_\sigma} (\boldsymbol{N}_i^{(h)}(\boldsymbol{x})\cdot\bar{\boldsymbol{t}})d\partial\Omega + \int_{\Omega} (\boldsymbol{N}_i^{(h)}(\boldsymbol{x})\cdot\boldsymbol{b})d\Omega \tag{14}$$

Here the column vector $\boldsymbol{N}_i^{(h)}(\boldsymbol{x})$ and $\boldsymbol{N}_j^{(h)}(\boldsymbol{x})$ are respectively the i-th and j-th column of $\boldsymbol{N}^{(h)}(\boldsymbol{x})$. The integrals of equations (13) and (14) are usually evaluated by Gauss quadrature over each element. Finally the boundary conditions (2) are applied and the linear system of equations is solved to find all the components of the vector $\boldsymbol{u}^{(h)}$.

2.4 Domain decomposition with consistent discretization

When a finite element discretization is used to solve the elastostatic problems over the subdomains Ω_1 and Ω_2 the interface will be discretized in the surfaces Γ_1^h and Γ_2^h. We call consistent discretization the case where the nodes of the interface are on the same positions for both subdomains Ω_1 and Ω_2 and the shape functions of each element on both sides of the interfaces are the same.
In this case the domain decomposition is not a concrete issue. In fact the communication between the degree of freedoms (DOFs) of the two discretization is straightforward. We can nevertheless introduce a partition of the DOFs that will be used for each of the latter approaches discussed in this work. We will call $\boldsymbol{u}_1^{(h)}, \boldsymbol{u}_2^{(h)}, \boldsymbol{u}_{\Gamma_1}^{(h)}, \boldsymbol{u}_{\Gamma_2}^{(h)}$ respectively the DOFs of nodes inside Ω_1 but not on the interface Γ_1, the DOFs of nodes inside Ω_2 but not on the interface Γ_2, the DOFs of the nodes of the interface Γ_1 and the DOFs of the nodes on the interface Γ_2. In the following the index (h) will be neglected for brevity. The discretized form of equations (8)-(9) is then:

$$\begin{bmatrix} \boldsymbol{K}_{1,1} & \boldsymbol{K}_{1,\Gamma_1} & \boldsymbol{0} & \boldsymbol{0} \\ \boldsymbol{K}_{\Gamma_1,1} & \boldsymbol{K}_{\Gamma_1,\Gamma_1} & \boldsymbol{0} & \boldsymbol{0} \\ \boldsymbol{0} & \boldsymbol{0} & \boldsymbol{K}_{\Gamma_2,\Gamma_2} & \boldsymbol{K}_{\Gamma_2,2} \\ \boldsymbol{0} & \boldsymbol{0} & \boldsymbol{K}_{2,\Gamma_2} & \boldsymbol{K}_{2,2} \end{bmatrix} \begin{Bmatrix} \boldsymbol{u}_1 \\ \boldsymbol{u}_{\Gamma_1} \\ \boldsymbol{u}_{\Gamma_2} \\ \boldsymbol{u}_2 \end{Bmatrix} = \begin{Bmatrix} \boldsymbol{f}_1 \\ \boldsymbol{f}_{\Gamma_1} + \boldsymbol{r}_{\Gamma_1} \\ \boldsymbol{f}_{\Gamma_2} + \boldsymbol{r}_{\Gamma_2} \\ \boldsymbol{f}_2 \end{Bmatrix} \tag{15}$$

[3] The standard Galerkin approximation is well established approach that produces a symmetric stiffness matrix consistent with the classic variational formulation, more generally the space of function of $\mathbb{U}^h$ and $\mathbb{V}^h$ may not be the same as it is the case for the Petrov-Galerkin methods.

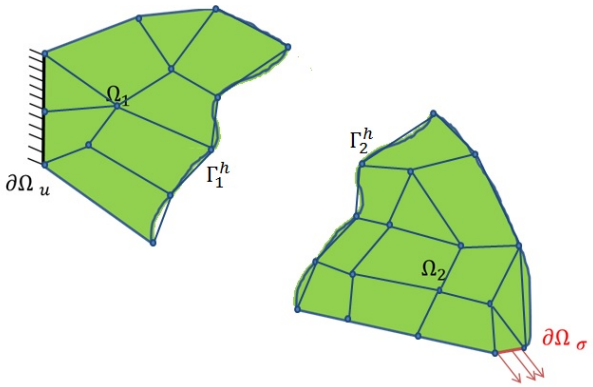

Fig. 3: Consistent discretization of the partitioned domain

The residuals $\boldsymbol{r}_{\Gamma_1}$ and $\boldsymbol{r}_{\Gamma_2}$ are the expression of the internal forces acting on the interface DOFs of each surface. Equations (6) and (7) are easily interpreted in this case since the node in the same position belonging to both meshes will merge and have the same DOFs. This can be expressed as:

$$\boldsymbol{u}_{\Gamma_2} = \boldsymbol{u}_{\Gamma_1} = \boldsymbol{u}_\Gamma \qquad \boldsymbol{r}_{\Gamma_2} = -\boldsymbol{r}_{\Gamma_1} \tag{16}$$

Where it is assumed that the interface DOFs have been sorted giving the same index to corresponding DOFs of corresponding nodes. Substituting equations (16) back into equation (15) and eliminating the residuals one can get:

$$\begin{bmatrix} \boldsymbol{K}_{1,1} & \boldsymbol{K}_{1,\Gamma_1} & \boldsymbol{0} \\ \boldsymbol{K}_{\Gamma_1,1} & \boldsymbol{K}_{\Gamma_1,\Gamma_1} + \boldsymbol{K}_{\Gamma_2,\Gamma_2} & \boldsymbol{K}_{\Gamma_2,2} \\ \boldsymbol{0} & \boldsymbol{K}_{2,\Gamma_2} & \boldsymbol{K}_{2,2} \end{bmatrix} \begin{Bmatrix} \boldsymbol{u}_1 \\ \boldsymbol{u}_\Gamma \\ \boldsymbol{u}_2 \end{Bmatrix} = \begin{Bmatrix} \boldsymbol{f}_1 \\ \boldsymbol{f}_{\Gamma_1} + \boldsymbol{f}_{\Gamma_2} \\ \boldsymbol{f}_2 \end{Bmatrix} \tag{17}$$

Obviousely, in the case of a conforming interface equation (17) could also be obtained using the conforming discretization of equation (5). Indeed equations (12) and (17) are equivalent.

3 Domain decomposition with non-consistent discretization

Cafiero et al. [15] shows different cases in which the non conforming discretization can increase the challenge associated with a ”transfer” of displacement field and stress tensor between meshes. In the following section the different scenarios are reviewed.

3.0.1 Non conformity scenarios

The first case we want to address is the simplest one (cf. figure 4). The interface boundary and area are the same, $\Gamma_1^h \equiv \Gamma_2^h$, the normal are opposite in each corresponding point of the interfaces. It may be the case for in the context of a domain decomposition for a multi-grid approach. The nodes are not in the same position but the shape functions of both domains are still the same. As a consequence, the local balance of the surface traction using a mortar approach will also imply the satisfaction of a patch test [59].

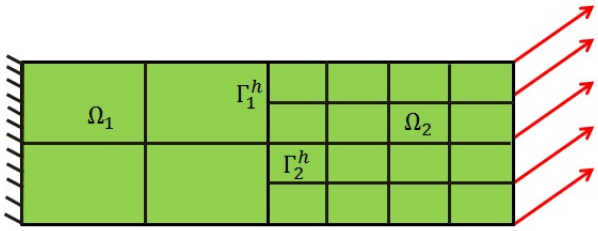

Fig. 4: Inconsistent mesh partition that do not introduce geometric inconsistency: $\Gamma_1^h \equiv \Gamma_2^h$

The second case is the first case of geometric inconsistency due to the non coincidence of the boundary of the interface (figure 5).

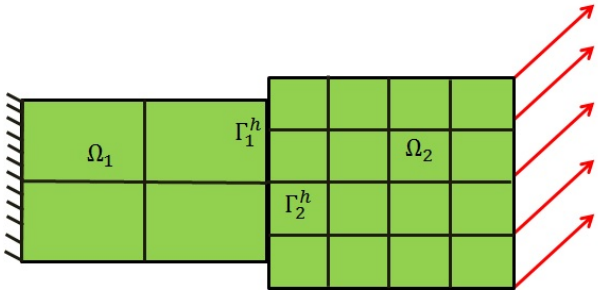

Fig. 5: Inconsistent mesh partition that introduces geometric inconsistency: $\Gamma_1^h \not\equiv \Gamma_2^h$, first case different mesh boundaries

Still the surface normal is the opposite that means that the patch test may be satisfied by the use of mortar approach. In figure 6 we present a second case that also produces a geometric inconsistency: wen a curved interface is discretized with non-matching meshes, the normal vectors are distinct on each element surface and may not be opposite for corresponding elements[4]. The area is different on both mesh surfaces. Moreover there can be a gap or intersections of interface mesh surfaces.
In this case the satisfaction of the patch test is only approximated with the use of the mortar approach [59]. Another important scenario is the one in figure 7 that shows two domains with the same node position but with different shape functions. Also in this case the normal and the geometry of the interpolated interfaces are not coincident, and special methods are needed to deal with this case [73].The most general scenario could be the combination of one or more of these scenarios, as it will be discussed later.

[4] In this case even the definition of corresponding elements is not straightforward. A possible definition is that two elements are corresponding if the area of the intersection between one element surface and the projection of the other element surface on the first one is positive and if the element center distance is less then a given tolerance

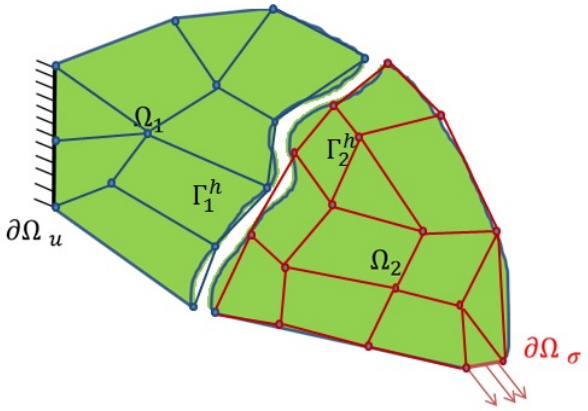

Fig. 6: Inconsistent mesh partition that introduces geometric inconsistency: $\Gamma_1^h \not\equiv \Gamma_2^h$, second case curbed interface

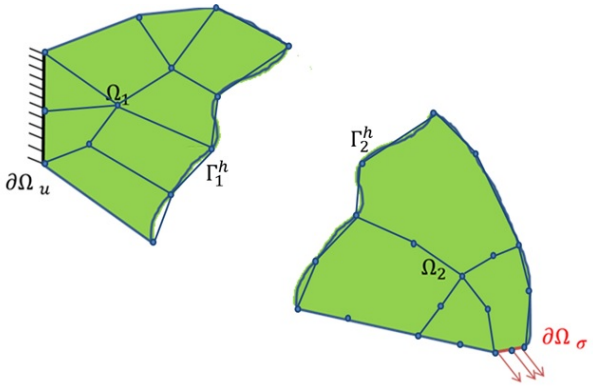

Fig. 7: Inconsistent mesh partition that introduces geometric inconsistency: $\Gamma_1^h \not\equiv \Gamma_2^h$, third case different shape functions

3.1 Elimination methods - Master/Slave approaches

This is a family of approaches that we can find described in Barlow et al. [4] and in the review paper of De Boer et al [23] that we briefly resume and complete in this section. The main idea consist in the reformulation of equations (6) and (7) as linear relationships between the interfaces of the sub-domains. Then one of the surfaces is chosen as slave (Γ_2), its DOFs will be explicitly given in function of the DOFs of the master surface (Γ_1).

$$\boldsymbol{u}_{\Gamma_2} = \boldsymbol{\Pi}_{21}\boldsymbol{u}_{\Gamma_1} \tag{18}$$

From a physical point of view the total work as the resultant force of the internal forces on the interface should be zero (energy conservation and static balance).

$$\boldsymbol{r}_{\Gamma_1}^T \cdot \boldsymbol{u}_{\Gamma_1} + \boldsymbol{r}_{\Gamma_2}^T \cdot \boldsymbol{u}_{\Gamma_2} = 0 \tag{19}$$

$$\mathbf{1}_{\Gamma_1}^T \cdot \boldsymbol{r}_{\Gamma_1} + \mathbf{1}_{\Gamma_2}^T \cdot \boldsymbol{r}_{\Gamma_2} = \mathbf{0} \tag{20}$$

In which $\mathbf{1}_{\Gamma_1}$ and $\mathbf{1}_{\Gamma_2}$ are matrix with number of line equal to the number of DOFs of interface Γ_1 and Γ_2 and 3 columns (one per each balance). For 3D solid elements they are Boolean matrices that have 1 on the component whose line correspond to the direction given by the index of their column and 0 otherwise. Equations (19) and (20) combined with equation (18) give:

$$\boldsymbol{r}_{\Gamma_1} = -\boldsymbol{\Pi}_{21}^T \boldsymbol{r}_{\Gamma_2} \tag{21}$$

$$\boldsymbol{\Pi}_{21} \mathbf{1}_{\Gamma_1} = \mathbf{1}_{\Gamma_2} \tag{22}$$

Equation (22) is a necessary condition that must be satisfied by the projection operator $\boldsymbol{\Pi}_{21}$ defined in equation (18). On the other hand, equation (21) is used with equations (15) and (16) to finally get the reduced system of equations:

$$\begin{bmatrix} \boldsymbol{K}_{1,1} & \boldsymbol{K}_{1,\Gamma_1} & \mathbf{0} \\ \boldsymbol{K}_{\Gamma_1,1} & \boldsymbol{K}_{\Gamma_1,\Gamma_1} + \boldsymbol{\Pi}_{21}^T \boldsymbol{K}_{\Gamma_2,\Gamma_2} \boldsymbol{\Pi}_{21} & \boldsymbol{\Pi}_{21}^T \boldsymbol{K}_{\Gamma_2,2} \\ \mathbf{0} & \boldsymbol{K}_{2,\Gamma_2} \boldsymbol{\Pi}_{21} & \boldsymbol{K}_{2,2} \end{bmatrix} \begin{Bmatrix} \boldsymbol{u}_1 \\ \boldsymbol{u}_{\Gamma_1} \\ \boldsymbol{u}_2 \end{Bmatrix} = \begin{Bmatrix} \boldsymbol{f}_1 \\ \boldsymbol{f}_{\Gamma_1} + \boldsymbol{\Pi}_{21}^T \boldsymbol{f}_{\Gamma_2} \\ \boldsymbol{f}_2 \end{Bmatrix} \tag{23}$$

That is a linear system of equation with a positive semi-definite symmetric matrix like the stiffness matrix of equation (12). The projection operator $\boldsymbol{\Pi}_{21}$ can be defined using two different approaches that in the contact community are known as node to segment and segment to segment approaches. In the former the relation between the DOFs is given directly by a geometric interpolation. De Boer et al. [23] show two examples of these methods: the Nearest neighbour interpolation (NN) [71] and the Radial Basis Functions (RBF) [6], [66]. Another option consists in using of the trace of element shape function on the interface to interpolate the displacement field. In this paper we will refer to these methods as Element Shape Function interpolation (ESF). The main drawback of these methods is their strong dependence on the slave and master surface choice. In fact for domains meshed with different mesh sizes, choosing the most refined mesh as master surface will not ensure the continuity of the displacement field for all the master nodes that do not belong to elements that contain a slave node projection. Moreover these methods don't satisfy simple patch tests even if the interface is not curved, and finally as it was shown by Bernardi et al. [7] they are sub-optimal in term of mesh convergence. The segment to segment approaches even if much more complicated can show better accuracy. In this section we present the last elimination method based on a weak form of the continuity equation: the Weighted Residual Methods (WRM).

3.1.1 Radial Basis Function interpolation (RBF)

For more general applications the RBF represent a practical and easy to implement solution. In this approach the displacement field at the interface is supposed to be a linear combination of radial basis functions defined per each node of the master surface:

$$\boldsymbol{u}_{\Gamma_1}(\boldsymbol{x}) = \sum_{s=1}^{N_{\Gamma_1}} \alpha_s \phi_s(\|\boldsymbol{x} - \boldsymbol{x}_s^{\Gamma_1}\|, r_s) + p(\boldsymbol{x}) \tag{24}$$

Here $\boldsymbol{u}_{\Gamma_1}$ is the displacement field on surface Γ_1. α_s is the weight relative to the s-th radial basis function ϕ_s, $\|\boldsymbol{x} - \boldsymbol{x}_s^{\Gamma_1}\|$ is the euclidean distance of point $\boldsymbol{x}$ from the node s-th node of the master surface Γ_1, $r_s \in \mathbb{R}$ is the shape factor of the s-th radial basis function ϕ_s , N_{Γ_1} is the number of nodes of Γ_1 and $p(\boldsymbol{x})$ is a polynomial function of $\boldsymbol{x}$. In this work $p(\boldsymbol{x})$ is not

considered, for a more general discussion of RBF the reader is referred to [23] , [6] and [66]. The weights α_s of equation (24) can be found using the interpolation conditions:

$$\boldsymbol{u}_{\Gamma_1}(\boldsymbol{x}_i^{\Gamma_1}) = u_{\Gamma_1 i} \ \forall i = 1,\ldots,N_{\Gamma_1} \tag{25}$$

As a consequence the weights factors will be

$$\boldsymbol{A} = \boldsymbol{\Phi}^{-1}\boldsymbol{u}_{\Gamma_1} \tag{26}$$

Where $\boldsymbol{\Phi}$ was defined as:

$$\boldsymbol{\Phi}_{i,j} = \phi_i(\|\boldsymbol{x}_j^{\Gamma_1} - \boldsymbol{x}_i^{\Gamma_1}\|, r_s) \tag{27}$$

Finally to impose the continuity of displacements at the interface (equation (16)) one can use the interpolation given by the RBF that takes the form:

$$\boldsymbol{u}_{\Gamma_2} = \boldsymbol{\Psi}^T \cdot \boldsymbol{A} = \boldsymbol{\Psi}^T \cdot \boldsymbol{\Phi}^{-1}\boldsymbol{u}_{\Gamma_1} = \boldsymbol{\Pi}_{21}\boldsymbol{u}_{\Gamma_1} \tag{28}$$

Here we defined the matrix Ψ as:

$$\Psi_{i,j} = \phi_i(\|\boldsymbol{x}_j^{\Gamma_2} - \boldsymbol{x}_i^{\Gamma_1}\|, r_s) \tag{29}$$

Different radial basis functions ($\phi(\cdot)$) can be found in the literature [74], [14] , [33]. An example considered in this work is the compactly supported functions B&W [74]:

$$\phi(\|\boldsymbol{x}\|, r_s) = \left(1 - \frac{\|\boldsymbol{x}\|}{r_s}\right)_+^4 \left(1 + 4\frac{\|\boldsymbol{x}\|}{r_s}\right) \tag{30}$$

A benchmark of the most popular RBF can be found in Deparis et al. [27]. The latter deals with the choice of the shape factor r_s in a local manner in order to find a good compromise between precision and evaluation cost ($\boldsymbol{\Phi}$ band width). In the same work the RBFs are rescaled in order to avoid spurious oscillation due to interpolation so that they satisfy the condition given by equation (22).

3.1.2 Element Shape Function interpolation (ESF)

A natural, but more complex, approachconsists in the projection of slave surface nodes on master surface elements. So that :

$$\Pi_{21i,j} = \boldsymbol{N}_j^{\Gamma_1}(\boldsymbol{x}_i^{\Gamma_2}) \tag{31}$$

Where $\boldsymbol{N}_j^{\Gamma_1}$ is the j-th column of the $\boldsymbol{N}^{(h)}(\boldsymbol{x})$ matrix of equation (11) for Γ_1 interface elements. This projection is quite simple for planar intefaces but for a general curved interfaces the projection may be more complicated. An elegant solution is presented in Puso et al. [60] who considered the normal vector in the center of master elements to rapidly evaluate the projection. For nearly planar surfaces this can be a reasonable approximation, on the other hand for double curved surfaces this approximation may not be justified. For each node (i) of Γ_1 and for each element (j) of Γ_2 we want to find the local coordinates (ξ_{ij}, η_{ij}) that describe the position of the node (i) on the surface Γ_j described by the element (j). In the case of geometrical inconsistency (figure 6) the node (i) may not lie on the surface Γ_j, in that case we want to find the local coordinates of the point of $(i^*) \in \Gamma_j$ (as in figure 8) that is the closest to (i) i.e.

$$min_{(\xi_j,\eta_j)} d_{ij}^2(\xi_j,\eta_j) = min_{(\xi_j,\eta_j)} \left(\|\boldsymbol{x}(\xi_j,\eta_j) - \boldsymbol{x}_{(i)}\|^2\right) \tag{32}$$

To find all the corresponding local coordinates of one mesh projected on the other this optimization problem has to be solved for all $N_{\Gamma_1}^{(e)} \times N_{\Gamma_2}$ pairs of nodes (i) element (j). To improve the numerical efficiency of this procedure the squared distance function may be summed up to build a function that has to be minimized once for each node (i) to get its local coordinate in each corresponding element $\boldsymbol{\Xi}, \boldsymbol{\Theta}$:

$$D_i^2(\boldsymbol{\Xi}, \boldsymbol{\Theta}) = \sum_{j=1}^{N_{\Gamma_1}^{(e)}} d_{ij}^2(\xi_j, \eta_j) \tag{33}$$

Moreover the gradient of each squared distance can be computed analytically to speed up the optimization convergence using a gradient based optimization algorithm for unconstrained problems for example the Quasi-Newtom algorithm [22, 24]- [25, 40].

$$\nabla d_{i,j}^2(\xi_j, \eta_j) = 2\nabla \boldsymbol{x}(\xi_j, \eta_j) \cdot \left(\boldsymbol{x}(\xi_j, \eta_j) - \boldsymbol{x}_{(i)}\right) \tag{34}$$

When this procedure is used, for convex interface meshes there may be nodes that are far

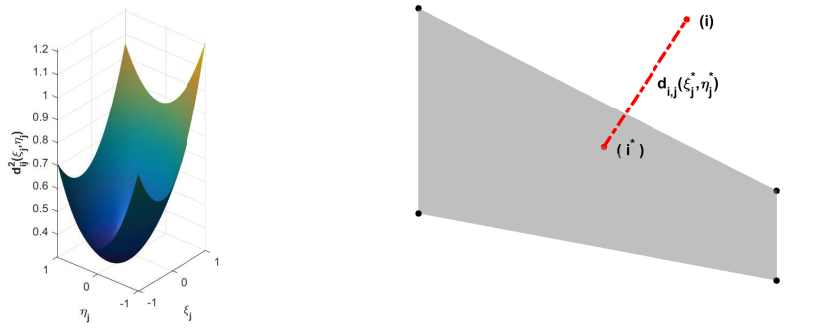

(a) Squared distance function

(b) Minimal distance configuration for a bi-linear quad element

Fig. 8: Node to element projection

from the element (j) but that have their corresponding point (i^*) inside the element (j). The shape function of equation 31 should take in account the minimal distance $d_{ij}\left(\xi_j^*, \eta_j^*\right)$: all the DOFs of the node (i) at a distance superior to a given tolerance t to its projection (i^*) on Γ_j , should not be considered dependent on the (j) elements DOFs i.e.:

$$\Pi_{21i,j} = \begin{cases} N_j^{\Gamma_1}(\xi^*, \eta^*) & d_{ij}\left(\xi_j^*, \eta_j^*\right) \leq t \\ 0 & otherwise \end{cases} \tag{35}$$

3.1.3 Weighted Residual Methods (WRM)

The methods described until now are based on a strong formulation of the continuity on the interface of the displacement field (equation 18). On the other hand, segment to segment

methods try to impose the continuity of displacement at the interface by the use of a weak form. One such method is the Weighted residual methods described in De Boer et al. [23], CebralĪ et al [16] and Löhner et al. [54] for the fluid-structure interaction problem.[5] In this approach the jump of the displacement field across the interface has to be orthogonal in the $\mathbb{L}_2$ sense to the trace on Γ_2 of the kinematic admissible virtual displacement $\boldsymbol{v} \in \mathbb{V}$:

$$\int_\Gamma \boldsymbol{v}(\boldsymbol{x}) \cdot (\boldsymbol{u}_{\Gamma_2}(\boldsymbol{x}) - \boldsymbol{u}_{\Gamma_1}(\boldsymbol{x}))\, d\Gamma = 0 \ \forall \boldsymbol{v} \in \mathbb{V} \tag{36}$$

Discretizing $\boldsymbol{v}(\boldsymbol{x})$ using the shape functions of Γ_2 and using equation (10) for each subdomains and writing one equation for each shape function of the discretized space $\mathbb{V}^h_{\Gamma_2}$ equation (36) becomes :

$$\boldsymbol{M}_2 \boldsymbol{u}_{\Gamma_2} - \boldsymbol{M}_{21} \boldsymbol{u}_{\Gamma_1} = \boldsymbol{0} \tag{37}$$

Where the mass matrices are defined as:

$$M_{2i,j} = \int_\Gamma \boldsymbol{N}_i^{\Gamma_2}(\boldsymbol{x}) \cdot \boldsymbol{N}_j^{\Gamma_2}(\boldsymbol{x}) d\Gamma \tag{38}$$

$$M_{21i,j} = \int_\Gamma \boldsymbol{N}_i^{\Gamma_2}(\boldsymbol{x}) \cdot \boldsymbol{N}_j^{\Gamma_1}(\boldsymbol{x}) d\Gamma \tag{39}$$

We can finally explicit the slave DOFs in function of the master DOFs as:

$$\boldsymbol{u}_{\Gamma_2} = \boldsymbol{M}_2^{-1} \boldsymbol{M}_{21} \boldsymbol{u}_{\Gamma_1} = \boldsymbol{\Pi}_{21} \boldsymbol{u}_{\Gamma_1} \tag{40}$$

It is shown in De Boer et al [23] that this method respects the condition of equation (22) therefore the force resultant is conserved at the interface. In order to evaluate the integral from equation (38) and (39) the support of the integral has to be chosen.

In fact in the most general case the surfaces described by the meshes will not be coincident and a projection will be needed (cf. figure (9)) [6]
One can observe that the integrand's support (cf. figure 10c)is $\Gamma_{j1^*k2} \equiv \Gamma_{j1^*} \cap \Gamma_{k2}$. The total support Γ is therefore the union of all the intersection of each Γ_{k2} with all corresponding projection Γ_{j1^*} of Γ_{j1} on Γ_{k2}:

$$\Gamma \equiv \cup_{k2=1}^{N_2^{(e)}} \cup_{j1=1}^{N_1^{(e)}} \Gamma_{j1^*k2} \tag{41}$$

For the numeric evaluation of $\boldsymbol{M}_2$ and $\boldsymbol{M}_{21}$ we were inspired by the procedure in Puso et al. [60]. Compared to Puso's original approach we implemented however some modifications in terms of node-to-element projection, and in terms of intersection polygon definition in order to render the procedure more robust. Instead of using the clipping algorithm of Foley [21] that may fail in some cases (see [41] for further details), we implemented the procedure described by Gander et al. in [41]. To obtain the intersection polygon Γ_{j1^*k2}, firstly the nodes $(s1)$ of Γ_{j1} that have a projection inside the element $(k2)$ are found. Secondly the nodes $(s2)$ of Γ_{k2} that are inside the projected element surface Γ_{j1^*} are found. Thirdly the intersection points $(s3)$ of all the sides of Γ_{k2} with the one of Γ_{j1^*}. The union of $(s1), (s2)$ and $(s3)$ form the vertices of the intersection polygon see figure 11a.
A triangulation of this polygon is obtained connecting all the sides with the polygon center.

[5] In these approaches it is avoid the use of Lagrange multipliers like in the Mortar methods ([7], [8]) anyway when the shape functions of Lagrange multipliers are the same of the displacement field of the slave surface, the consequent equations are the same as it is also shown in Jeon et al. [47]

[6] Note that Γ_{j1}^* sides are generally curbed, in this work they are considered to be straights, this approximation will affect the accuracy of the evaluation of $\mathbf{M_{21}}$. in equation (39). Nevertheless the error induced by this approximation can be considered negligible

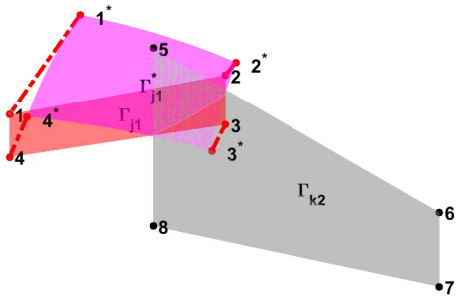

(a) Elements belonging to inconsistent meshes of the same interface surface.

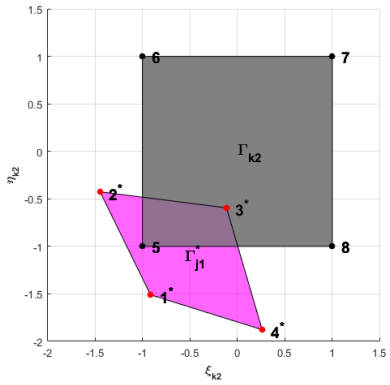

(b) Projected master element on slave element surface in slave local coordinates.

Fig. 9: Element to element projection examples. The master element surface Γ_{j1} has been projected on the slave element surface Γ_{k2} using the same procedure shown in figure (8) for each node of the element $j1$ $(1,2,3,4)$. In this way it possible to obtain the projected slave surface Γ^*_{j1} $(1^*,2^*,3^*,4^*)$. The union of the projection of all the element of Γ_1 on Γ_2 is then indicated as Γ_1^*. After this projection a change in local variables (ξ_{k2},η_{k2}) of the element $k2$ can be employed for the evaluation of Mass matrices (equations (38) and (39))

Finally 3 Gauss points per pallet have to be used for the numerical integration of equation (38) and (39)) (see the example of figure 11b). The Gauss point local coordinates $(\boldsymbol{\Xi}_{k2}^{(GP)},\boldsymbol{\Theta}_{k2}^{(GP)})$ are easy to find in function of the triangulation coordinates. On the other hand, to know the value of $\boldsymbol{N}_j^{\Gamma_1}$ on the corresponding points of Γ_{j1^*} for equation (39)), the local coordinates $(\boldsymbol{\Xi}_{j1}^{(GP)},\boldsymbol{\Theta}_{j1}^{(GP)})$ have to be determined. Puso suggested even for this projection to use the normal of element $(k2)$ on the center of the element. To be completely rigorous one should evaluate the normal to the surface Γ_{k2} in each Gauss point and then make an intersection of the line on witch the normal lies and the surface of Γ_{j1} to finally have the local coordinates $(\boldsymbol{\Xi}_{j1}^{(GP)},\boldsymbol{\Theta}_{j1}^{(GP)})$. In other words we should find the roots of the

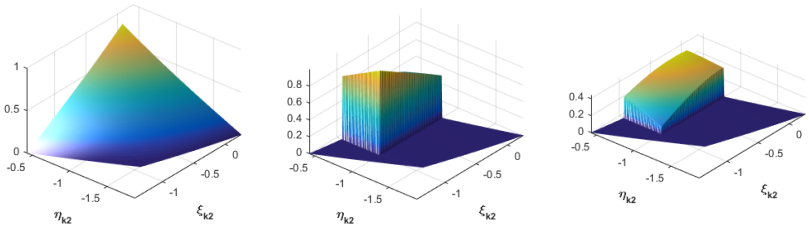

(a) $N_{3^*}(\xi_{k2},\eta_{k2})$ (b) $N_5(\xi_{k2},\eta_{k2})$ (c) $N_{3^*}(\xi_{k2},\eta_{k2})\cdot N_5(\xi_{k2},\eta_{k2})$

Fig. 10: Shape function of node 3^* of $j1$, of node 5 of $k2$ for the example of figure 9 and their product that has to be integrated in equation (39), are represented.

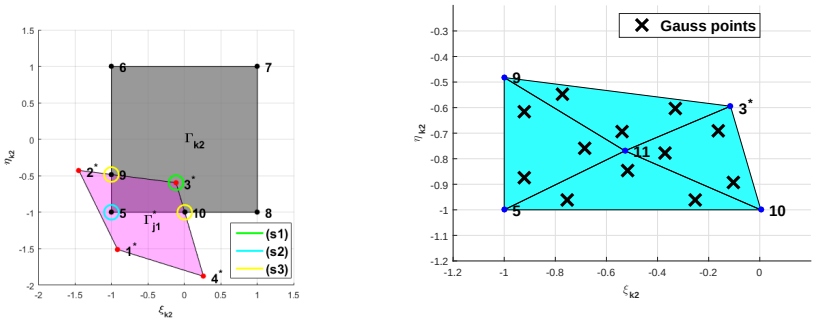

(a) Determination of Γ_{j1^*k2} vertex. (b) Integration over Γ_{j1^*k2}

Fig. 11: Procedure for the determination of Γ_{j1^*k2} vertex and consequent numerical integration

non linear system of equations:

$$2\nabla \boldsymbol{x}_{\Gamma_{k2}}\left(\boldsymbol{\Xi}_{k2}^{(GP)},\boldsymbol{\Theta}_{k2}^{(GP)}\right)\cdot\left(\boldsymbol{x}_{\Gamma_{k2}}\left(\boldsymbol{\Xi}_{k2}^{(GP)},\boldsymbol{\Theta}_{k2}^{(GP)}\right)-\boldsymbol{x}_{\Gamma_{j1}}\left(\boldsymbol{\Xi}_{j1}^{(GP)},\boldsymbol{\Theta}_{j1}^{(GP)}\right)\right)=\mathbf{0} \tag{42}$$

Taking in consideration the fact that the side of Γ_{j1^*} are considered as straight segment between the projection on Γ_{k2} of the nodes of $(j1)$, even if this is not always the case, the use of equation (42) is not recommended. Some Gauss points when re-projected on Γ_{j1} could lie outside the element $(j1)$. To avoid this situation a geometric isoparametric interpolation between the local coordinate (ξ_{j1},η_{j1}) and the projected one (ξ_{k2},η_{k2}) is considered here:

$$\xi_{k2}(\xi_{j1},\eta_{j1})=\xi_{k2}^{1^*}N_1(\xi_{j1},\eta_{j1})+\xi_{k2}^{2^*}N_2(\xi_{j1},\eta_{j1})+\xi_{k2}^{3^*}N_3(\xi_{j1},\eta_{j1})+\xi_{k2}^{4^*}N_4(\xi_{j1},\eta_{j1}) \tag{43}$$

$$\eta_{k2}(\xi_{j1},\eta_{j1})=\eta_{k2}^{1^*}N_1(\xi_{j1},\eta_{j1})+\eta_{k2}^{2^*}N_2(\xi_{j1},\eta_{j1})+\eta_{k2}^{3^*}N_3(\xi_{j1},\eta_{j1})+\eta_{k2}^{4^*}N_4(\xi_{j1},\eta_{j1}) \tag{44}$$

Where $(\xi_{k2}^{n^*}, \xi_{k2}^{n^*})$ are the local coordinates of the projection of the n-th node of $(j1)$ on Γ_{k2} and N_n are the classic bilinear shape function:

$$\begin{aligned} N_1(\xi_{j1},\eta_{j1}) &= \tfrac{1}{4}(1-\xi_{j1})(1-\eta_{j1}) \\ N_2(\xi_{j1},\eta_{j1}) &= \tfrac{1}{4}(1-\xi_{j1})(1+\eta_{j1}) \\ N_3(\xi_{j1},\eta_{j1}) &= \tfrac{1}{4}(1+\xi_{j1})(1+\eta_{j1}) \\ N_4(\xi_{j1},\eta_{j1}) &= \tfrac{1}{4}(1+\xi_{j1})(1-\eta_{j1}) \end{aligned} \tag{45}$$

Finally equation (43)-(44) can be used to find $(\boldsymbol{\Xi}_{j1}^{(GP)}, \boldsymbol{\Theta}_{j1}^{(GP)})$ solving another non linear system of equations:

$$\boldsymbol{\Xi}_{k2}^{(GP)} - \xi_{k2}\left(\boldsymbol{\Xi}_{j1}^{(GP)}, \boldsymbol{\Theta}_{j1}^{(GP)}\right) = \mathbf{0} \tag{46}$$

$$\boldsymbol{\Theta}_{k2}^{(GP)} - \eta_{k2}\left(\boldsymbol{\Xi}_{j1}^{(GP)}, \boldsymbol{\Theta}_{j1}^{(GP)}\right) = \mathbf{0} \tag{47}$$

This system can be solved numerically (e.g. with a Newton-Raphson algorithm) giving the analytical expression of the Jacobian matrix. In figure 12 the Gauss points are projected from Γ_{j1*k2} back on Γ_{j1} using the iso-parametric projection of equations (46)-(47)

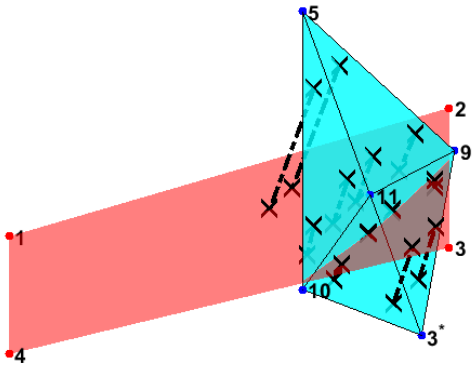

Fig. 12: Gauss point projection

3.2 Variational based approaches

In variational approaches, instead of using the principle of virtual work to get the final system of equations, the displacement field solution of the static problem will be sought to minimize the total energy:

$$E(\boldsymbol{u}) = \boldsymbol{u}^T \boldsymbol{K}\boldsymbol{u} - \boldsymbol{u}^T \boldsymbol{f} \tag{48}$$

Considering the partition that we already introduced the total energy becomes:

$$E(\boldsymbol{u}_1,\boldsymbol{u}_{\Gamma_1},\boldsymbol{u}_{\Gamma_2},\boldsymbol{u}_2)=\left\{\begin{array}{cccc}\boldsymbol{u}_1^T & \boldsymbol{u}_{\Gamma_1}^T & \boldsymbol{u}_{\Gamma_2}^T & \boldsymbol{u}_2^T\end{array}\right\}\left(\left[\begin{array}{cccc}\boldsymbol{K}_{1,1} & \boldsymbol{K}_{1,\Gamma_1} & \boldsymbol{0} & \boldsymbol{0}\\ \boldsymbol{K}_{\Gamma_1,1} & \boldsymbol{K}_{\Gamma_1,\Gamma_1} & \boldsymbol{0} & \boldsymbol{0}\\ \boldsymbol{0} & \boldsymbol{0} & \boldsymbol{K}_{\Gamma_2,\Gamma_2} & \boldsymbol{K}_{\Gamma_2,2}\\ \boldsymbol{0} & \boldsymbol{0} & \boldsymbol{K}_{2,\Gamma_2} & \boldsymbol{K}_{2,2}\end{array}\right]\left\{\begin{array}{c}\boldsymbol{u}_1\\ \boldsymbol{u}_{\Gamma_1}\\ \boldsymbol{u}_{\Gamma_2}\\ \boldsymbol{u}_2\end{array}\right\}-\left\{\begin{array}{c}\boldsymbol{f}_1\\ \boldsymbol{f}_{\Gamma_1}\\ \boldsymbol{f}_{\Gamma_2}\\ \boldsymbol{f}_2\end{array}\right\}\right) \tag{49}$$

Note that in equation (49) the work at the interface of the residual is eliminated for energy conservation. The system of equations that comes from this formulation has a singular matrix, so that the solution of the static problem cannot be simply obtained by minimizing the total energy.

3.2.1 Mortar Element Method

The basic idea of the Mortar approach is to add a dislocation potential to the total energy, in order to impose the continuity of the displacement field at the interface:

$$E_d(\boldsymbol{u},\boldsymbol{\lambda})=\int_{\Gamma}\boldsymbol{\lambda}\left(\boldsymbol{u}|_{\Gamma_1}-\boldsymbol{u}|_{\Gamma_2}\right)d\Gamma \tag{50}$$

This potential is summed with the total energy to get the Lagrangian functional $E_l(\boldsymbol{u},\boldsymbol{\lambda})=E_d(\boldsymbol{u},\boldsymbol{\lambda})+E(\boldsymbol{u})$ whose stationary points are the solution of the constrained optimization:

$$\begin{cases} min_{\boldsymbol{u}}(E(\boldsymbol{u}))\\ \boldsymbol{u}|_{\Gamma_1}-\boldsymbol{u}|_{\Gamma_2}=0\end{cases} \tag{51}$$

Similarly to Master/Slave approaches, the mortar approach needs the choice of one surface to be the mortar surface and the other to be the non-mortar. The interpolation functions of the lagrangian multipliers $\boldsymbol{\lambda}$ are (in the case of two domains) chosen to be the same as those of the slave surface:[7]

$$\boldsymbol{\lambda}(\boldsymbol{\lambda}|_{\Gamma_2})=\boldsymbol{N}(\boldsymbol{\lambda}|_{\Gamma_2})\boldsymbol{\lambda}_{\Gamma_2} \tag{52}$$

The dislocation potential can then be written as:

$$E_d(\boldsymbol{u}_{\Gamma_1},\boldsymbol{u}_{\Gamma_2},\boldsymbol{\lambda}_{\Gamma_2})=\boldsymbol{\lambda}_{\Gamma_2}^T\left(\boldsymbol{M}_{21}\boldsymbol{u}_{\Gamma_1}-\boldsymbol{M}_2\boldsymbol{u}_{\Gamma_2}\right) \tag{53}$$

Then the Lagrangian functional is stationary for:

$$\left[\begin{array}{ccccc}\boldsymbol{K}_{1,1} & \boldsymbol{K}_{1,\Gamma_1} & \boldsymbol{0} & \boldsymbol{0} & \boldsymbol{0}\\ \boldsymbol{K}_{\Gamma_1,1} & \boldsymbol{K}_{\Gamma_1,\Gamma_1} & \boldsymbol{M}_{21}^T & \boldsymbol{0} & \boldsymbol{0}\\ \boldsymbol{0} & \boldsymbol{M}_{21} & \boldsymbol{0} & -\boldsymbol{M}_2 & \boldsymbol{0}\\ \boldsymbol{0} & \boldsymbol{0} & -\boldsymbol{M}_2^T & \boldsymbol{K}_{\Gamma_2,\Gamma_2} & \boldsymbol{K}_{\Gamma_2,2}\\ \boldsymbol{0} & \boldsymbol{0} & \boldsymbol{0} & \boldsymbol{K}_{2,\Gamma_2} & \boldsymbol{K}_{2,2}\end{array}\right]\left\{\begin{array}{c}\boldsymbol{u}_1\\ \boldsymbol{u}_{\Gamma_1}\\ \boldsymbol{\lambda}_{\Gamma_2}\\ \boldsymbol{u}_{\Gamma_2}\\ \boldsymbol{u}_2\end{array}\right\}=\left\{\begin{array}{c}\boldsymbol{f}_1\\ \boldsymbol{f}_{\Gamma_1}\\ \boldsymbol{0}\\ \boldsymbol{f}_{\Gamma_2}\\ \boldsymbol{f}_2\end{array}\right\} \tag{54}$$

Even if the equations obtained from this approach seem to be different from the one of the WRM eliminating the Lagrange eigenvalues from equation (54) we can recognize that they have the same solution (see Jeong et al. [47] for the proof). It can be noted that this method has the same difficulties of implementation and of evaluation cost encountered with the WRM method: The integral of the shape function over the intersection of the interface has to be evaluated in order to evaluate the mass matrices $\boldsymbol{M}_{21},\boldsymbol{M}_2$. The Mortar approach is shown to be as precise as the WRM approach with a quite bigger effort due to the increased number of variables. For this reason in section 4 only WRM has been implemented and compared with other methods.

[7] In the work of Puso et al [60] the dual space is also employed

3.3 The Internodes Approach

Here we describe the internodes approach, introduced for the first time by Deparis et al in [26] and further analyzed by Gervasio et al in [42]. We derived it's matrix formulation directly from equation (8). Like in the elimination approaches the continuity of the displacement field is guaranteed by equation (18). On the other hand the balance of energy and efforts are not imposed. The forces $\boldsymbol{t}_{12}$ and $\boldsymbol{t}_{12}$ are supposed to be interpolated with the same shape functions of displacement on each subdomain interface:

$$\boldsymbol{t}_{12}(\boldsymbol{x}|_{\Gamma_2}) = \boldsymbol{N}^{(h)}(\boldsymbol{x}|_{\Gamma_2})\boldsymbol{p}_2 \tag{55}$$

$$\boldsymbol{t}_{21}(\boldsymbol{x}|_{\Gamma_1}) = \boldsymbol{N}^{(h)}(\boldsymbol{x}|_{\Gamma_1})\boldsymbol{p}_1 \tag{56}$$

Conforming with these definitions the residual at the interface may be evaluated as:

$$\boldsymbol{r}_{\Gamma_1} = \int_{\Gamma_1} \boldsymbol{N}^{(h)}(\boldsymbol{x}|_{\Gamma_1}) \cdot \boldsymbol{N}^{(h)}(\boldsymbol{x}|_{\Gamma_1})\boldsymbol{p}_1 d\Gamma_1 = \boldsymbol{M}_1\boldsymbol{p}_1 \tag{57}$$

$$\boldsymbol{r}_{\Gamma_2} = \int_{\Gamma_2} \boldsymbol{N}^{(h)}(\boldsymbol{x}|_{\Gamma_2}) \cdot \boldsymbol{N}^{(h)}(\boldsymbol{x}|_{\Gamma_2})\boldsymbol{p}_2 d\Gamma_2 = \boldsymbol{M}_2\boldsymbol{p}_2 \tag{58}$$

The balance of the internal forces per unit area is imposed in a similar fashion to the continuity of the displacement as in equation (18), but this time a second interpolation operator is used:

$$\boldsymbol{p}_1 + \boldsymbol{\Pi}_{12}\boldsymbol{p}_2 = \boldsymbol{0} \tag{59}$$

Substituting equation (57) and (58) in (59) one gets:

$$\boldsymbol{r}_{\Gamma_1} + \boldsymbol{M}_1\boldsymbol{\Pi}_{12}\boldsymbol{M}_2^{-1}\boldsymbol{r}_{\Gamma_2} = \boldsymbol{r}_{\Gamma_1} + \boldsymbol{Q}_{12}\boldsymbol{r}_{\Gamma_2} = \boldsymbol{0} \tag{60}$$

Finally, using equations (60) and (18) in (8) one can get:

$$\begin{bmatrix} \boldsymbol{K}_{1,1} & \boldsymbol{K}_{1,\Gamma_1} & \boldsymbol{0} \\ \boldsymbol{K}_{\Gamma_1,1} & \boldsymbol{K}_{\Gamma_1,\Gamma_1} + \boldsymbol{Q}_{12}\boldsymbol{K}_{\Gamma_2,\Gamma_2}\boldsymbol{\Pi}_{21} & \boldsymbol{Q}_{12}\boldsymbol{K}_{\Gamma_2,2} \\ \boldsymbol{0} & \boldsymbol{K}_{2,\Gamma_2}\boldsymbol{\Pi}_{21} & \boldsymbol{K}_{2,2} \end{bmatrix} \begin{Bmatrix} \boldsymbol{u}_1 \\ \boldsymbol{u}_{\Gamma_1} \\ \boldsymbol{u}_2 \end{Bmatrix} = \begin{Bmatrix} \boldsymbol{f}_1 \\ \boldsymbol{f}_{\Gamma_1} + \boldsymbol{Q}_{12}\boldsymbol{f}_{\Gamma_2} \\ \boldsymbol{f}_2 \end{Bmatrix} \tag{61}$$

It can be observed that the system of equation of the internodes formulation is not symmetric and that equation (21) and (22) are not imposed so that internodes is not a conservative method. On the other hand the formulation and the implementation are straightforward if compared with the mortar and the WRM approaches: the only mass matrices $\boldsymbol{M}_2$, $\boldsymbol{M}_1$ and the interolation operators $\boldsymbol{\Pi}_{12}$ and $\boldsymbol{\Pi}_{21}$ are needed. Good convergence property have been showed in the work of Gervasio et al. [42].

3.4 Weighted Average Continuity Approach (WACA)

The collocation approaches even if simple are not precise enough when the the most refined mesh is chosen as master surface. On the other hand the segment to segment approaches are very accurate but are complex and need much more computational effort. The Internodes approach seeks to achieve such a trade-off between complexity and accuracy but, as it will be shown in section 4, the fact that it does not conserve the resultant force vector and total energy at the interface can deteriorate its accuracy. We would like to develop a new method here that shares with Internodes its simplicity but achieve an improved accuracy. This one is based on another expression of the continuity of the displacement field at the interface.

Before we introduce the new formulation let us highlight some equations that can be derived. Each line of the vector coming from the multiplication of the interface mass matrix and the interface displacement vector represent the integral over the interface of the displacement field times the shape function of the DOF corresponding to the selected line. We can define a weighted average displacement field using as weight the shape function as:

$$\bar{u}_{\Gamma_1 i} = \frac{\int_{\Gamma_1} \boldsymbol{u}(\boldsymbol{x}\|_{\Gamma_1}) \cdot \boldsymbol{N}_i^{\Gamma_1}(\boldsymbol{x}\|_{\Gamma_1}) d\Gamma_1}{\int_{\Gamma_1} (\boldsymbol{N}_i^{\Gamma_1}(\boldsymbol{x}\|_{\Gamma_1}))_i d\Gamma_1} \tag{62}$$

That can be reformulated as:

$$(M_1 u_{\Gamma_1})_i = S_{N_i} \bar{u}_{\Gamma_1 i} \tag{63}$$

Where S_{N_i} is the integral of the i-th shape function over its support and $\bar{u}_{\Gamma_1 i}$ is the weighted average of the i-th displacement on Γ_1. We can put this relationship in the matrix form:

$$\boldsymbol{M}_1 \boldsymbol{u}_{\Gamma_1} = \boldsymbol{S}_1 \bar{\boldsymbol{u}}_{\Gamma_1} \qquad \boldsymbol{M}_2 \boldsymbol{u}_{\Gamma_2} = \boldsymbol{S}_2 \bar{\boldsymbol{u}}_{\Gamma_2} \tag{64}$$

Where we indicate with $\boldsymbol{S}_1$ and $\boldsymbol{S}_2$ the diagonal matrices containing on the diagonal the integral of each shape function on its support[8], and with $\bar{\boldsymbol{u}}_{\Gamma_1}$ and $\bar{\boldsymbol{u}}_{\Gamma_2}$ the weighted average displacement field of each component over the corresponding shape function support. In the approach we propose we seek to state the continuity of the weighted average displacement interpolating between the two surface i.e.

$$\bar{\boldsymbol{u}}_{\Gamma_2} = \boldsymbol{\Pi}_{21} \bar{\boldsymbol{u}}_{\Gamma_1} \tag{65}$$

By substitution of equation (64) into equation (65) one gets a new interpolation operator between the displacement field:

$$\boldsymbol{u}_{\Gamma_2} = \boldsymbol{M}_2^{-1} \boldsymbol{S}_2 \boldsymbol{\Pi}_{21} \boldsymbol{S}_1^{-1} \boldsymbol{M}_1 \boldsymbol{u}_{\Gamma_1} = \boldsymbol{\Pi}_{21}^* \boldsymbol{u}_{\Gamma_1} \tag{66}$$

If the interpolation operator $\boldsymbol{\Pi}_{21}$ satisfies the conservation conditions given by equation (22), $\boldsymbol{\Pi}_{21}^*$ will also satisfy the same conditions:

$$\begin{aligned} \boldsymbol{\Pi}_{21}^* \mathbf{1}_{\Gamma_1} = \boldsymbol{M}_2^{-1} \boldsymbol{S}_2 \boldsymbol{\Pi}_{21} \boldsymbol{S}_1^{-1} \boldsymbol{M}_1 \mathbf{1}_{\Gamma_1} = \boldsymbol{M}_2^{-1} \boldsymbol{S}_2 \boldsymbol{\Pi}_{21} \boldsymbol{S}_1^{-1} \boldsymbol{S}_1 \mathbf{1}_{\Gamma_1} = \\ = \boldsymbol{M}_2^{-1} \boldsymbol{S}_2 \boldsymbol{\Pi}_{21} \mathbf{1}_{\Gamma_1} = \boldsymbol{M}_2^{-1} \boldsymbol{S}_2 \mathbf{1}_{\Gamma_2} = \boldsymbol{M}_2^{-1} \boldsymbol{M}_2 \mathbf{1}_{\Gamma_2} = \mathbf{1}_{\Gamma_2} \end{aligned} \tag{67}$$

Where we used twice the fact that the mass coherent and lumped mass matrices conserve the sum of lines i.e.

$$\boldsymbol{M}_1 \mathbf{1}_{\Gamma_1} = \boldsymbol{S}_1 \mathbf{1}_{\Gamma_1} \qquad \boldsymbol{M}_2 \mathbf{1}_{\Gamma_2} = \boldsymbol{S}_2 \mathbf{1}_{\Gamma_2} \tag{68}$$

The condition of zero work at the interface (equation 19) can be used as was done in the classic elimination methods so that the final matrix form of the WACA approach is:

$$\begin{bmatrix} \boldsymbol{K}_{1,1} & \boldsymbol{K}_{1,\Gamma_1} & \boldsymbol{0} \\ \boldsymbol{K}_{\Gamma_1,1} & \boldsymbol{K}_{\Gamma_1,\Gamma_1} + (\boldsymbol{\Pi}_{21}^*)^T \boldsymbol{K}_{\Gamma_2,\Gamma_2} \boldsymbol{\Pi}_{21}^* & (\boldsymbol{\Pi}_{21}^*)^T \boldsymbol{K}_{\Gamma_2,2} \\ \boldsymbol{0} & \boldsymbol{K}_{2,\Gamma_2} \boldsymbol{\Pi}_{21}^* & \boldsymbol{K}_{2,2} \end{bmatrix} \begin{Bmatrix} \boldsymbol{u}_1 \\ \boldsymbol{u}_{\Gamma_1} \\ \boldsymbol{u}_2 \end{Bmatrix} = \begin{Bmatrix} \boldsymbol{f}_1 \\ \boldsymbol{f}_{\Gamma_1} + (\boldsymbol{\Pi}_{21}^*)^T \boldsymbol{f}_{\Gamma_2} \\ \boldsymbol{f}_2 \end{Bmatrix} \tag{69}$$

This formulation shares the same simplicity of the Internodes approach, on the other hand satisfies *a priori* the conservation of the residual sum at the interface and of the energy at the interface.

[8] $\boldsymbol{S}_1$ and $\boldsymbol{S}_2$ are also indicated as lumped mass matrix

3.5 *A priori* conservation of moments

All the methods proposed here do respect the balance of residual resultant and residual work but do not respect an *a priori* condition on the moments of the resultant at the interface. In the work of Puso [60] to enforce this balance of moments and keep the same formulation of the mortar method the nodes of slave surface in the undeformed configuration are moved on the interface surface. This method is interesting but still not very practical to conserve the meshes of both sub-domains. Another interesting approach is proposed by Park et al. in [59], were a third surface and mesh (the frame) are introduced and the balance of moments and of the patch test are satisfied choosing the position of nodes on the frame. To the authors' best knowledge no works exist which propose to respect the moments' balance equation through an *a priori* condition on the interpolation operators Π_{12}, Π_{21}. This is the objective of this subsection in which a necessary condition is determined and used to correct the projection operator for all eliminations methods as well as for the new WACA method. First of all lets write the balance of moments of the residual:

$$\sum_{i=1}^{n_{\Gamma_1}} \boldsymbol{OP}_{i\Gamma_1} \times \boldsymbol{R}_{i\Gamma_1} + \sum_{j=1}^{n_{\Gamma_2}} \boldsymbol{OP}_{j\Gamma_2} \times \boldsymbol{R}_{j\Gamma_2} = \boldsymbol{0} \tag{70}$$

We defined here $\boldsymbol{OP}_{i\Gamma_s}$ as the vector connecting the fixed point O to the positions of the i^{th} nodes of Γ_s surface (s=1,2); $\boldsymbol{R}_{i\Gamma_s}$ as the vector of the residual force at the same node. This equation must be satisfied for each possible combination of residual. For the energy balance (21) the residuals are not independent so that all the combination of residuals can be obtained as all the vectors in $\boldsymbol{R}^{N_{\Gamma_2}}$ where $N_{\Gamma_2} = n_d n_{\Gamma_2}$ is the number of DOFs of the second interface. Satisfying equation (70) for all vectors of $\boldsymbol{R}^{N_{\Gamma_2}}$ means that it has to be verified for each vector in a normal basis, for example the canonical one. For each node j and for each direction $n_d^{(j)}$ (for each k_2 DOF) we can then write 3 equations as follows:

$$\sum_{i=1}^{n_{\Gamma_1}} \boldsymbol{OP}_{i\Gamma_1} \times \left(\boldsymbol{R}_{i\Gamma_1}\right)_{n_d^{(i)}} + \boldsymbol{OP}_{j\Gamma_2} \times \left(\boldsymbol{R}_{j\Gamma_2}\right)_{n_d^{(j)}} = \boldsymbol{0} \quad \forall k_2 \in \{1,2,\ldots,N_{\Gamma_2}\} \tag{71}$$

By the use of (21) on can replace $\left(\boldsymbol{R}_{i\Gamma_1}\right)_{n_d^{(i)}}$ by the $(k_2, \boldsymbol{k_1})$ terms of $\boldsymbol{\Pi}_{21}$, that we will denote here as $\left(\boldsymbol{\Pi}_{21}\right)_{(k_2,\boldsymbol{k_1})}$, where the $\boldsymbol{k_1}$ are the index of the DOFs of the i^{th} node of Γ_1. Choosing $O \equiv P_{j\Gamma_2}$ to write each moments equations, equation (71) becomes:

$$\sum_{i=1}^{n_{\Gamma_1}} \boldsymbol{P}_{j\Gamma_2}\boldsymbol{P}_{i\Gamma_1} \times \left(\boldsymbol{\Pi}_{21}\right)^T_{(k_2,\boldsymbol{k_1})} = \boldsymbol{0} \quad \forall k_2 \in \{1,2,\ldots,N_{\Gamma_2}\} \tag{72}$$

This equation can be also written in the following matrix form:

$$\left(\boldsymbol{\Pi}_{21}\right)_{k_2} \cdot \boldsymbol{B}_{k2} = \boldsymbol{0} \qquad \forall k_2 \in \{1,2,\ldots,N_{\Gamma_2}\} \tag{73}$$

Where $\left(\boldsymbol{\Pi}_{21}\right)_{k_2}$ is the k_2^{th} line of $\boldsymbol{\Pi}_{21}$, $\boldsymbol{B}_{k2}$ is a matrix $N_{\Gamma_1} \times 3$ defined by:

$$\left(\boldsymbol{B}_{k2}\right)_{(k_1,n_d)} = \left(\boldsymbol{P}_{j\Gamma_2}\boldsymbol{P}_{i\Gamma_1} \times \boldsymbol{n}_{\boldsymbol{d}}^{(k_1)}\right)_{n_d} \tag{74}$$

$\boldsymbol{n}_{\boldsymbol{d}}^{(k_1)}$ is the 3×1 versor of the k_1^{th} DOF direction and by $(\bullet)_{n_d}$ the extraction of the n_d component of a vector. Equation 73 and equation 22 form a system of 6 equation for each line of the projecting operator that can be compactly written as:

$$\left(\boldsymbol{\Pi}_{21}\right)_{k_2} \cdot \boldsymbol{A}^T_{k_2} = \left(\boldsymbol{\Pi}_{21}\right)_{k_2} \cdot \left[\, \boldsymbol{1}_{\Gamma_1} \;\; \boldsymbol{B}_{k2} \,\right] = \left[\, \left(\boldsymbol{1}_{\Gamma_2}\right)_{k_2} \;\; \boldsymbol{0} \,\right] = \boldsymbol{b}^T \tag{75}$$

We seek to correct the projecting operator coming from an elimination approach (RBF, WRM, WACA) to respect equation (75). Since we don't want to significantly modify the previous interpolations, we would like to have a new line $(\boldsymbol{\Pi}_{21})_{k_2}^{(c)}$ that is as close as possible to the original one $(\boldsymbol{\Pi}_{21})_{k_2}$ and that satisfies equation 75. In other terms we want to solve the optimization problem

$$\begin{cases} min_{\boldsymbol{s}} \left(\boldsymbol{s} - (\boldsymbol{\Pi}_{21})_{k_2}\right)^T \cdot \left(\boldsymbol{s} - (\boldsymbol{\Pi}_{21})_{k_2}\right) \\ \boldsymbol{s} \cdot \boldsymbol{A}_{k_2}^T = \boldsymbol{b}^T \end{cases} \tag{76}$$

Here we indicated $(\boldsymbol{\Pi}_{21})_{k_2}^{(c)}$ as $\boldsymbol{s}$ for brevity. To solve this constrained optimization problem the Lagrangian approach can be used. The stationary condition of the Lagrangian form a linear system of equation that can be solved to find $\boldsymbol{s}^T$ as:

$$\left((\boldsymbol{\Pi}_{21})_{k_2}^{(c)}\right)^T = (\boldsymbol{\Pi}_{21})_{k_2}^T + \boldsymbol{A}_{k_2}^T \cdot (\boldsymbol{A}_{k_2} \cdot \boldsymbol{A}_{k_2}^T)^{-1} (\boldsymbol{b} - \boldsymbol{A}_{k_2} \cdot (\boldsymbol{\Pi}_{21})_{k_2}^T) \tag{77}$$

The resulting operator $\boldsymbol{\Pi}_{21}^{(c)}$ will then respect both the balance of resultant of residual/energy and moments. Still its precision in term of displacement and stress continuity could be affected so in the next section we will analyze its numerical efficiency. The correction presented here can be adapted even for the Internodes approach. The corrected scheme will modify the column of the $\boldsymbol{Q}_{12}$ and not the line of $\boldsymbol{\Pi}_{21}$. The resulting scheme will therefore conserve the balance of forces and moments but not of energy since $\boldsymbol{Q}_{12}^{(c)} \neq \boldsymbol{\Pi}_{21}^T$.

4 Benchmarking on numerical test cases

4.1 Test cases definition and analysis for consistent meshes

In this section we present two test case geometries, each investigated under pure traction and bending-traction boundary conditions, which will serve for benchmarking various methods considered. The first case is a column like structure with spherical ends see figure 13a. In the second case (figure 13b) the bottom structure is wider and shorter then the upper one and both ends are spherical. Both structures are completely fixed at the bottom face and for the pure traction loading they are loaded on the upper surface with a constant surface traction in the z direction of magnitude 30.25 MPa. The analysis made for configuration (1) is actually very similar to the ones frequently studied in the literature (cf. [68]). The main differences consist in the clamping on the bottom side and in curved instead of planar upper and bottom faces. Note that in configuration 2 our test problem does not have a closed form solution and we had to consider the fine and consistent mesh as reference for the analysis. One should also keep in mind that none of the presented methods passes linear patch tests for curved interfaces.However, the classic constant stress patch test is not a necessary condition for optimality convergence [70] and other conditions have to been proposed in the Generalized patch test [69] or in the FEM test [64] . On the other hand one could be wondering how much the error induced by the violation of the patch test can affect a general solution. The following benchmarking will try to bring some insights to this question.
In the FEM, the upper and the lower domains are meshed with linear brick finite elements with complete quadrature (8 Gauss points). In configuration (1) in figure 13a the upper and the lower domains are meshed with $10 \times 10 \times 10$ and $10 \times 10 \times 20$ elements respectively. Configuration (1) represents a very simple configuration and we also sought a more general

case in witch the interface surfaces do not have the same boundaries. To achieve this we considered configuration (2), see figure 13b. In this case the nodes that are not inside the boundary of the intersection of the interface surfaces have to be eliminated from the interface node set. To find these nodes one has to check the interpolation operator (applicable for RL-RBF but also for ES) looking for all-zero columns and all-zero lines and eliminate the corresponding nodes from the set of interface node. This avoids major errors of projection and gives much better results for all the methods considered. In configuration (2) in figure 13b the upper domain is meshed in the same way and the lower domain with $20 \times 20 \times 5$ elements. The total active DOFs are 10890 in configuration (1) and 10245 in configuration (2). These configurations are denoted in the rest of this paper as reference configurations and will serve for comparison, since they involve consistent meshes between the upper and lower domains and involve the most refined meshes.

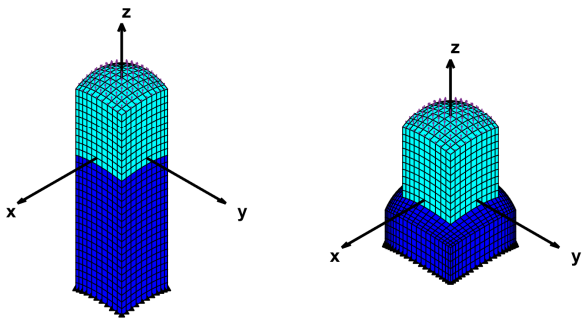

(a) Geometric configuration (1) (b) Geometric configuration (2)

Fig. 13: Geometric configurations (1) and (2), pure traction load case

In figure 14 a bending-traction loading condition is applied to both geometrical configurations. In this case we simply added a second surface traction component in the x direction with the same magnitude as the one in z direction (30.25MPa). The upper and the lower domains are meshed with consistent meshes, so that this analysis does not introduce any interpolation error between the meshes. The displacement field corresponding to the pure traction and to the bending-traction loadings are represented in figure 15 and 16 respectively.

The finite element code (in house code, implemented in Matlab) used for this test has been tested and validated with a comparison with Abaqus 6.14. One can observe that in these configurations the displacement field is continuous at the interface between the upper and the lower domain. To represent the Von Mises stress, that is evaluated at each gauss integration point a global least square interpolation approach [45] was adopted (cf. figure 17 and 18). One can observe that for these meshes in both configurations the Von Mises stress is continuous at the interface. These configurations are denoted in the rest of this paper as reference configurations and will serve for comparison, since they involve consistent meshes between the upper and lower domains and involve the most refined meshes. Note also that

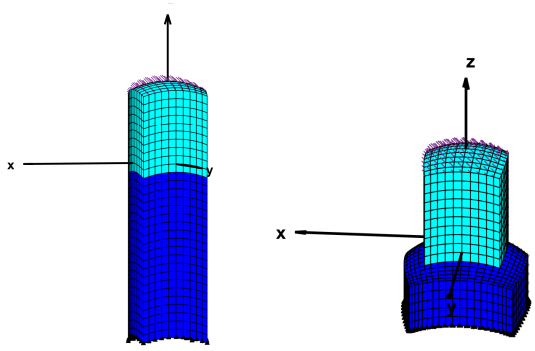

(a) Geometric configuration (1) (b) Geometric configuration (2)

Fig. 14: Geometric configurations (1) and (2), bending-traction traction load case

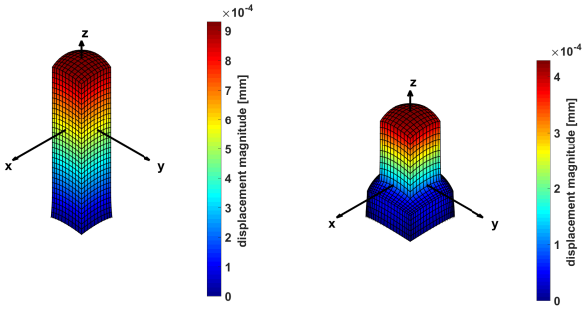

(a) Geometric configuration (1) (b) Geometric configuration (2)

Fig. 15: Displacement amplitude under pure traction load case

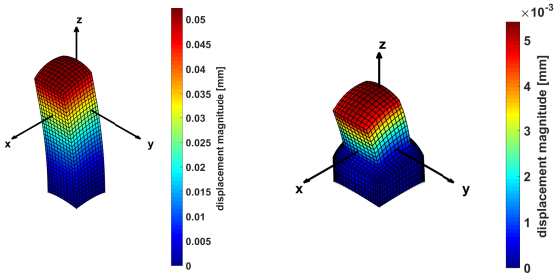

(a) Geometric configuration (1) (b) Geometric configuration (2)

Fig. 16: Displacement amplitude under bending-traction load case

the choice of the corresponding mesh densities was based on a convergence study, presented in Appendix 1.

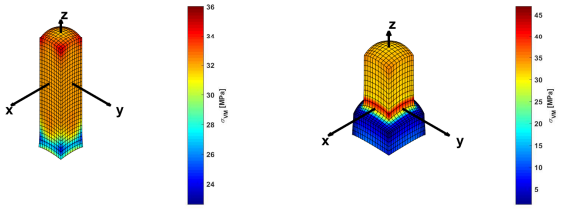

(a) Geometric configuration (1) (b) Geometric configuration (2)

Fig. 17: Von Mises stress under pure traction load case

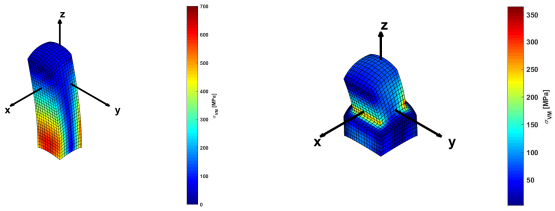

(a) Geometric configuration (1) (b) Geometric configuration (2)

Fig. 18: Von Mises stress under bending-traction load case

4.2 Benchmark Results

The inconsistent meshes that are tested here are obtained by changing the mesh of the bottom domain and keeping constant the mesh of the upper domain. The upper domain will always be a $(10 \times 10 \times 10)$ domain, on the other hand the bottom domain will change its mesh as $(n \times n \times 20)$ for configuration (1) and as $(m \times m \times 5)$ in the configuration (2), with n and m varying.
One can observe that in configuration (1) we are in the scenario of figure 6. On the other hand in configuration (2) both the inconsistency of figure 5 and 6 are encountered. To measure the quality of a given mesh tying technique, several parameters are studied as a function of the discretization of each domain:

– The interface must be in balance of force and moments. The sum of the residuals at one side must be the opposite value of the sum of residuals on the other side. The same for

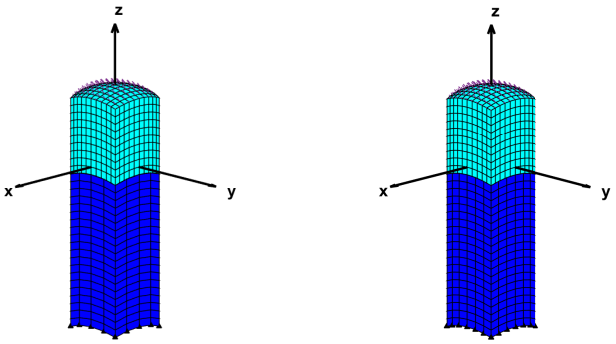

(a) Geometric configuration (1) $n = 4$ (b) Geometric configuration (1) $n = 6$

Fig. 19: Configuration (1) example of inconsistent meshes

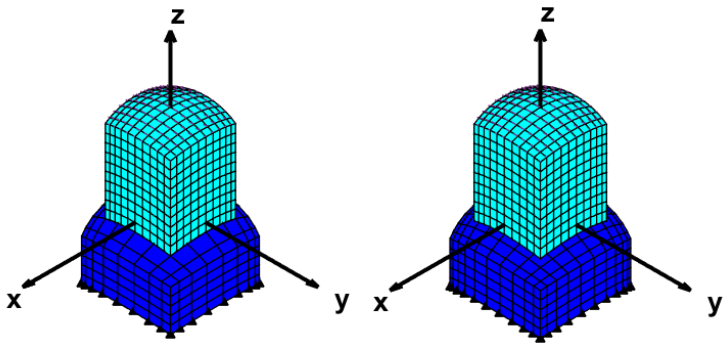

(a) Geometric configuration (2) $m = 8$ (b) Geometric configuration (2) $m = 10$

Fig. 20: Configuration (2) example of inconsistent meshes

the moments. We introduce the percent resultant force and moments relative error as:

$$E_R = \frac{\|\boldsymbol{R}_{\Gamma_1} + \boldsymbol{R}_{\Gamma_2}\|}{\|\boldsymbol{R}_{\Gamma_1}\|} \times 100\% \quad E_M = \frac{\|\mathscr{M}_{\Gamma_1} + \mathscr{M}_{\Gamma_2}\|}{\|\mathscr{M}_{\Gamma_1}\|} \times 100\% \tag{78}$$

Where we define as $\boldsymbol{R}_{\Gamma_i}$ the vector of the sum of the residual on the interface Γ_i, and $\mathscr{M}_{\Gamma_i}$ as the sum of residual moments around a fix point (in our case the origin).

– In the same way also the total work of the internal forces at the interface should vanish. For this reason one must also consider the compliance error as:

$$E_c = \left| \frac{\boldsymbol{r}_{\Gamma_1}^T \boldsymbol{u}_{\Gamma_1} + \boldsymbol{r}_{\Gamma_2}^T \boldsymbol{u}_{\Gamma_2}}{\boldsymbol{r}_{\Gamma_1}^T \boldsymbol{u}_{\Gamma_1}} \right| \times 100\% \tag{79}$$

– The displacement field has to be continuous at the interface. An indicator of displacement discontinuity can be considered as:

$$E_d = \left(\frac{\|\boldsymbol{u}_{\Gamma_1} - \boldsymbol{\Pi}_{12}\boldsymbol{u}_{\Gamma_2}\|}{2\|\boldsymbol{u}_{\Gamma_1}\|} + \frac{\|\boldsymbol{u}_{\Gamma_2} - \boldsymbol{\Pi}_{21}\boldsymbol{u}_{\Gamma_1}\|}{2\|\boldsymbol{u}_{\Gamma_2}\|} \right) \times 100\% \tag{80}$$

This indicator quantifies the amplitude of gaps and com-penetrations at both interface mesh nodes.

– If $m \leq 20$ and $n \leq 10$ the conforming meshes can be considered as reference solutions. We can then compare the displacement field at the node of the constant mesh side (upper domain) with the one in the conforming cases figure 13 and 14.

$$E_U = \frac{1}{N_{\Gamma_1}} \sum_{i=1}^{N_{\Gamma_1}} \frac{\|\boldsymbol{u}_{\Gamma_1 i} - \boldsymbol{u}_{\Gamma_1 i}^{ref}\|}{\|\boldsymbol{u}_{\Gamma_1 i}^{ref}\|} \times 100\% \tag{81}$$

N_{Γ_1} indicates the number of nodes of Γ_1 (interface surface of the upper domain) and $\boldsymbol{u}_{\Gamma_1 i}$ is the displacement vector in the i-th node of the same surface. The drawback of these indicators is that they are affected by the discretization in each sub-domain as well as they are affected by the interface interpolation.

– The convergence trough reference Von Mises stress can also be studied comparing upper domain gauss point stresses with the corresponding one in reference configuration. Once again the upper domain is unchanged as are its Gauss point locations. The average and the maximum Von Mises stress relative error over the entire upper domain Gauss points are studied.

$$E_S = \frac{1}{N_{PG_1}} \sum_{i=1}^{N_{PG_1}} \frac{|\boldsymbol{\sigma}_i - \boldsymbol{\sigma}_i^{ref}|}{|\boldsymbol{\sigma}_i^{ref}|} \times 100\% \tag{82}$$

$$E_\sigma = \max_i \left(\frac{|\boldsymbol{\sigma}_i - \boldsymbol{\sigma}_i^{ref}|}{|\boldsymbol{\sigma}_i^{ref}|} \times 100\% \right) \tag{83}$$

Where N_{PG_1} is the number of Gauss integration points in the upper domain finite elements.

– To complete the comparison the evaluation time will also be considered for each approach.

Different combinations can be adopted using methods described in section 3, For conciseness here we will concentrate only on a few methods:

– Re-Localized Radial Basis Function (RL-RBF) interpolation operator as described in subsection 3.1.1
– Weighted residual method (WRM) as described in subsection 3.1.3 this approach has the same accuracy of Mortar of subsection 3.2.1 but is less expensive in terms of computational effort due to the reduced number variables. Since the solution of the WRM method has been proven to have the same solution as the Mortar method (cf. [47]) we will use the label "WRM/Mortar" throughout the benchmark results.

- The Internodes as described in subsection 3.3 and RL-RBF interpolation operators.
- the Weighted Average Continuity Approach (WACA) following the description of subsection 3.4 also using the same RL-RBF interpolation operators.

For the benchmarking of these methods in configuration (1), the mesh refinement n of the bottom domain is made varying between 4 and 10. The choice of Master and Slave surfaces is also varied and both loading conditions (pure traction and bending-traction) are considered. Furthermore the application or not of the proposed moment correction approach is also considered. Similarly for configuration (2) the mesh refinement of the bottom domain m is varied between 8 a and 20.The detailed results of the parametric studies for configurations (1) and (2) are provided in Appendix 2. In order to summarize these parametric studies presented in the appendix we provide here in the main section, box plots that aggregate the error measures for all the different cases considered, cf. Fig. 21. In these plots the results are grouped by method and application of moment correction. The labeling "corrected methdod" means that the proposed moment correction was applied to the respective method. For recall, the line in the middle of the box is the median while the edges of the box represent the 25% and 75% percentiles. The whiskers extend to the most extreme data points not considered outliers, and the outliers are plotted individually by crosses in the plot.
Several conclusions can be drawn from the plots of Fig. 21. A priori moment correction not only makes it possible to satisfy the exact balance of moments as it is clear from figure 21b, moreover it sensibly improves the accuracy of all elimination approaches in terms of stress and displacements discrepancy (cf. figures 21d,21e,21f and 21g). For the computation time on the other hand this projection can cost less then the 25% of the overall CPU time, but improved implementation based on the use of matrices could further reduce this cost.
Overall the most accurate method is found to be WRM/Mortar, which is in accordance with the literature. Unfortunately, as often noted in the literature as well, the accuracy of the WRM/Mortar approach comes at the expense of a significant implementation complexity and significant computational cost (cf. Fig. 21h) . This is due to the fact that the WRM/Mortar method needs the tedious element to element projections and integrations for the mass matrix assembly that are not necessary in the other approaches. In De Boer the WRM method was described as ineffective for fluid structure applications with curved interfaces. Here we show that for elastostatic problems this method does not suffer of this weakness. The three other methods (RL-RBF, Internodes and WACA) have much lower implementation complexity and computational cost but come with different tradeoffs with respect to accuracy. The Internodes method does not appear to be able to achieve the vanishing of the work of the internal forces at the interface (cf. Fig. 21c), but this does not appear to necessarily badly affect the accuracy of the displacement field, compared to the other methods.
While on the majority of error metrics all methods appear to perform reasonably well, especially after balance of moments correction, one of the most discriminating error metrics is the discrepancy in the Von Mises stresses, where relatively large errors can still be encountered. In order to obtain a better overview of the actual discrepancy in terms of stresses we plot the stress maps corresponding to each approach before and after moment correction, for $n = 4$ and when Γ_1 (resp. Γ_2) is chosen as master surface in Fig. 22 (resp. in Fig.23). Artificial stress concentration are generated by the mesh coupling at the interface especially for RL-RBF, Internodes and WACA (even after moment correction). Note however that the *a priori* balance of moments correction sensibly improves the accuracy of the stress fields for all the methods which performed very poorly without this correction. It is also important to note that outliers can have totally unacceptable accuracy in terms of stresses. Overall, in

terms of accuracy of the stress field, we can note that the corrected WACA approach allows to achieve, on average, a low error on the stresses and a low dispersion from case to case, as well as less extreme outliers, making it a pertinent alternative to the WRM/Mortar approach, while involving a lower implementation complexity and computational cost. Several other additional conclusions can be drawn based on the detailed study of the dependence of the error measures with mesh density (see figures 26-29). In configuration (1)(figure 26) we can make following observations:

- n=10 is not represented for clarity, nevertheless we verified that all the error indicators were equal to 0 for n=10.
- In Figure 26a, and 26c one can check that RL-RBF,WACA and WRM/Mortar respecting equations (21) and (22) consequently conserve force resultant and elastic energy at the interface. On the other hand Internodes, that does not respect these equations, shows a discrepancy in terms of reaction sum and residual work at the interface. This discrepancy is severe when the difference between element areas at the interface is important (n=4-7) and when the coarser mesh (always Γ_2 in our study) is the master. Moreover the discrepancy becomes more severe when the load case is combined (bending-traction load case).
- None of the methods studied here conserve *a priori* the interface total moment(figure 26b). WACA and internodes do not conserve the moments for coarse meshes and in the combined load case. WRM/Mortar and RL-RBF perform better and seem to be reasonably accurate even for coarser mesh size. Of course for the pure traction case all the methods perform well in terms of zero moment conservation.
- In figure 26d we find that RL-RBF generate openings in the deformed configuration when the interface with the finest mesh (Γ_1 in our case) is the master. This is a classic problem of node to segment approaches. WACA improves the continuity of the displacement field but is less precise than internodes and WRM/Mortar especially in the combined load case. All these methods focus on the displacement field.
- In figure 26e,26f and 26g one can observe displacements and stress convergence at the upper domain[9] to the reference configuration (finest mesh tested with consistent mesh on the interface).We find that WRM/Mortar is quite accurate even for coarse meshes. The other methods are reasonably accurate for finer meshes.
- From figure 26e, 26b and 26g one can also observe that both WACA and internodes loose their precision in bending-traction load case. The non conservation of moments may be a cause of this weaknesses in agreements of accuracy improvements obtained after moment correction.
- In figure 26h we can see that WRM/Mortar is much slower (almost an order of magnitude) than the other methods, and this difference of cost increases with the problem size and with the interface refinement. The particular implementation chosen for this work has not been optimized to reduce the computational cost, anyway in all implementation the tedious element to element projection is the main source of computational effort.
- In figure 26d for n=5 for WACA,Internodes and RL-RBF, when Γ_2 is master $E_d\%$ is 0 to the machine precision. This is due to the fact that for this mesh all the nodes of Γ_2 are superposed to one node of Γ_1. For that reason choosing the coarsest mesh surface (Γ_2) as master will also imply the point-wise continuity on each node of (Γ_1). This is not the case for WRM/Mortar as the continuity is imposed in an integral form.

[9] As mentioned before we considered the error average over interface (Γ_1) nodes for displacement and the average over all the upper domain Gauss points for stress

The same study was conducted for configuration (2) (figure 27). Here can make following observations:

- In this case as well consistent mesh accuracy ($m = 20$) is not represented for clarity purpose nevertheless it has been checked that all errors converge to 0 in this configuration.
- The accuracy is much better when m is a multiple of 4 ($m = 8, 12, 16, 20$) i.e. when Γ_1 and Γ_2 have the same boundaries like in figure 20a. For all other configurations, the error is much higher for all the methods studied. The fact that some elements are cut by the interface boundaries like (cf. figure 20b) affects the precision of all the studied methods.
- The error in the total moments balance (figure 27b) is much smaller in this case for all methods except for Internodes where also the energy and the total reaction as indicated in figures 27a and 27c is much higher. Not having exactly the same area of element in both meshes is probably the main cause of this error.
- In terms of displacement continuity at the interface (cf. figures 27d) , the RL-RBF is this time overtaken by both WACA and Internodes.It must be noted that $E_d\%$ is small when both interfaces have similar displacement even if this is not the "good" one. RL-RBF poor accuracy is traduced in gap appearing at the interface in the deformed configuration especially in pure traction load case.
- Looking at the displacement and stress convergence to the reference solution (figures 27f and 27g respectively) WRM/Mortar confirms its accuracy even in this case. On the other hand Internodes and RL-RBF show poor convergence especially for $m \neq 8, 12, 16, 20$. WACA lies somewhere in between WRM/Mortar and Internodes.
- The CPU time in seconds (figure 27h) is still much higher for the WRM, for the same reason as in configuration (1).
- As was highlighted for configuration (1), looking at figures 27b , 27e and 27g a method seems to lose its accuracy for the stress prediction when the total moments balance at the interface is not respected.

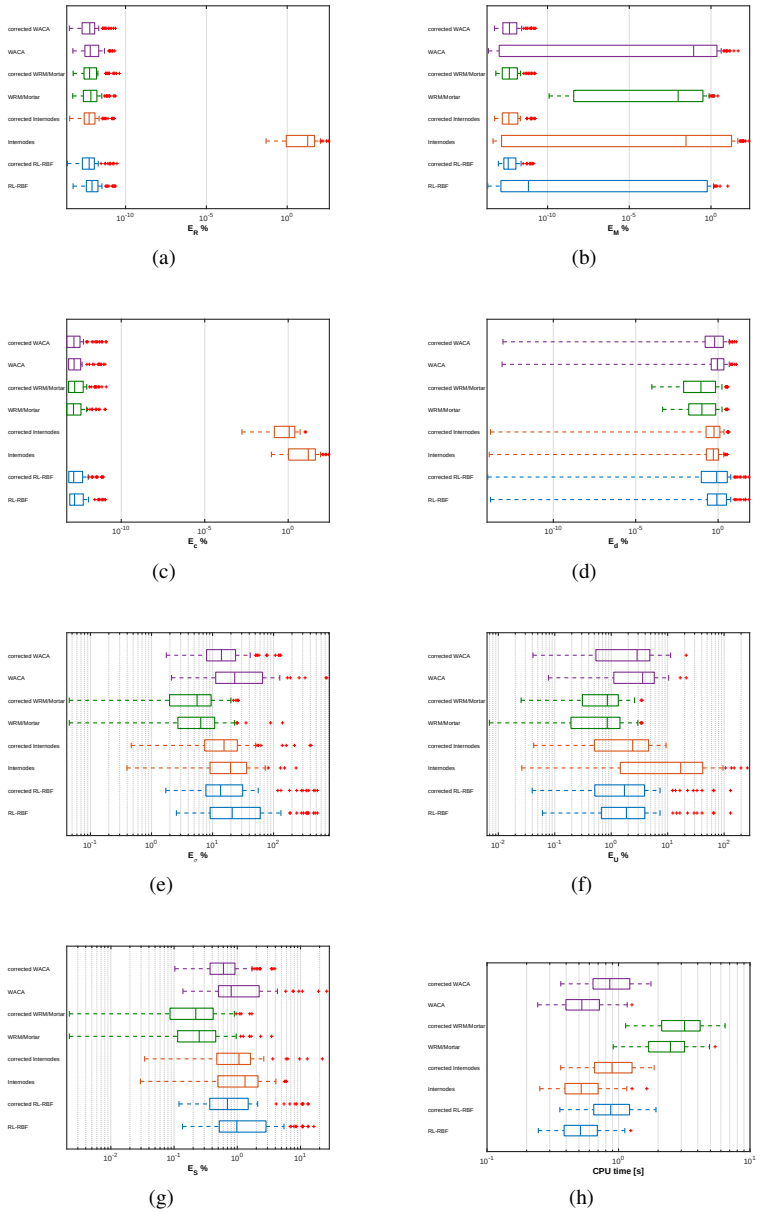

Fig. 21: Results accuracy and time dispersion over the whole test battery: (a) Boxplot of E_R, the Resultant Force relative error, (b) Boxplot of E_M, the moment relative error, (c) Boxplot of E_c, the interface compliance relative error, (d) Boxplot of E_d, the displacement discontinuity relative error, (e) Boxplot of E_σ, the maximum of Von Mises stress relative error, (f) Boxplot of E_U, interface displacement field relative error, (g) Boxplot of E_S, average Von Mises stress relative error, (h) Boxplot of CPU time (s);

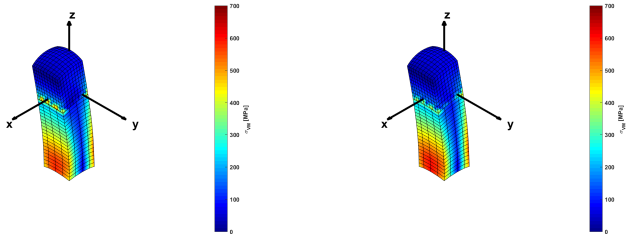

(a) WACA (b) Corrected WACA

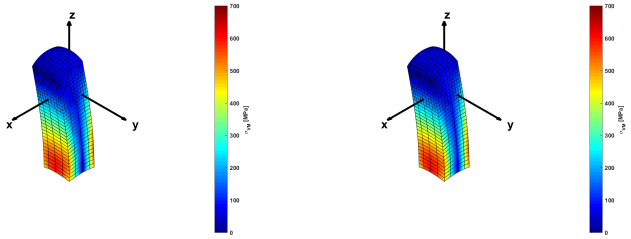

(c) WRM/Mortar (d) Corrected WRM/Mortar

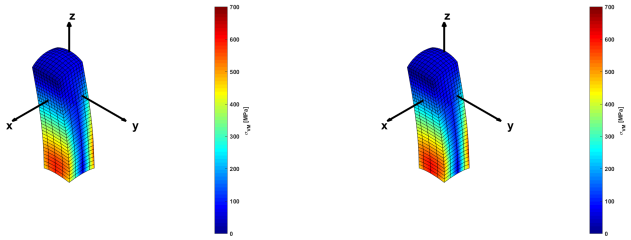

(e) Internodes (f) Corrected Internodes

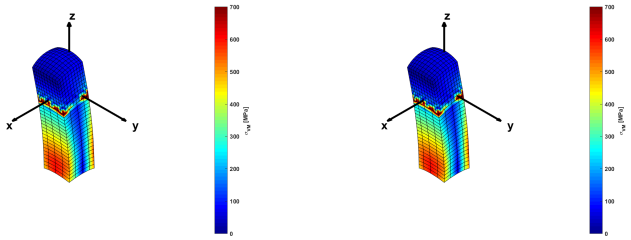

(g) RL-RBF (h) Corrected RL-RBF

Fig. 22: Von Mises stress plot configuration (1) under bending-traction load case, for $n = 4$ and Γ_1 master.

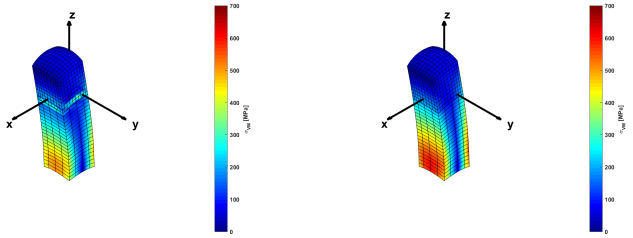

(a) WACA (b) Corrected WACA

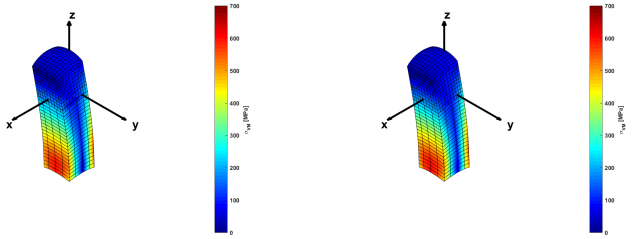

(c) WRM/Mortar (d) Corrected WRM/Mortar

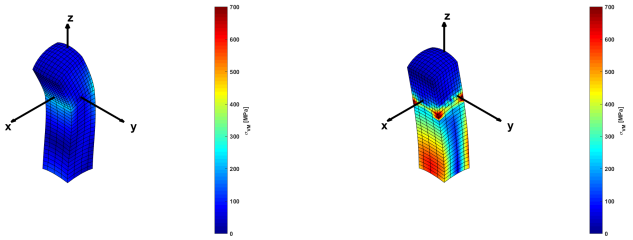

(e) Internodes (f) Corrected Internodes

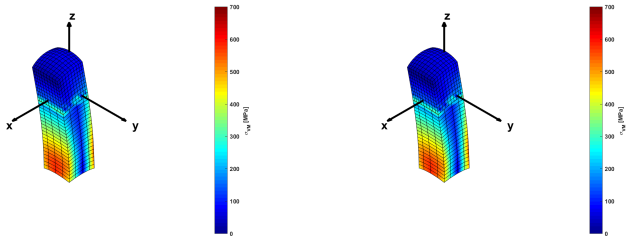

(g) RL-RBF (h) (h): Corrected RL-RBF

Fig. 23: Von Mises stress plot configuration (1) under bending-traction load case, for $n = 4$ and Γ_2 master.

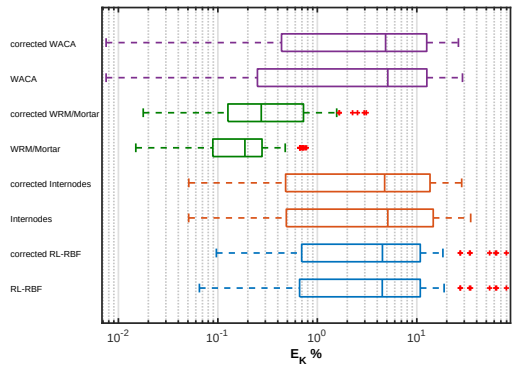

Fig. 24: Boxplot of E_K, interface specific kinetic energy relative error.

There is a last point on which we would like to comment. In this paper we focused just on elasto-static problem, so we didn't check for the continuity of the specific kinetic energy at the interface. Moving to a dynamic problem a relevant error measure is the continuity of the specific kinetic energy at the interface that can be written as:

$$\boldsymbol{u}_{\Gamma_1}^T \boldsymbol{M}_1 \boldsymbol{u}_{\Gamma_1} = \boldsymbol{u}_{\Gamma_2}^T \boldsymbol{M}_2 \boldsymbol{u}_{\Gamma_2} \tag{84}$$

We made a check of this continuity using the specific kinetic energy error index $E_k\%$ defined as:

$$E_k = \frac{\boldsymbol{u}_{\Gamma_1}^T \boldsymbol{M}_1 \boldsymbol{u}_{\Gamma_1} - \boldsymbol{u}_{\Gamma_2}^T \boldsymbol{M}_2 \boldsymbol{u}_{\Gamma_2}}{\boldsymbol{u}_{\Gamma_1}^T \boldsymbol{M}_1 \boldsymbol{u}_{\Gamma_1}} \times 100\% \tag{85}$$

Figure 24 results of all previous experiences are given also for $E_K\%$. We can see from these box-plots that further developments are still possible aimed at improving the accuracy of the methods for dynamic problems.

5 Conclusion and perspectives

In this paper we presented several techniques for mesh tying of inconsistently discretized domains. The Re-Localized Radial Basis Function interpolation (RL-RBF), The Weighted Residual Method/Mortar (WRM/Mortar), the Internodes were presented and a first contribution consisted in the proposal of the Weighted Average Continuity Approach (WACA). All these approaches were benchmarked comparing several accuracy metrics as well as CPU time. Note that we also proposed some implementation improvements for the WRM/Mortar method in order to make the approach more robust. Based on the benchmarking analysis we can confirm that WRM/Mortar is the most accurate approach for all indicators in terms of stress and displacement predictions. On the other hand it is the most complex method implemented here and also the most expensive in term of CPU time. The other methods involve much lower implementation complexity and computational cost but represent different trade-offs between the various error measures: displacements, stresses, interface forces and moments, total work at the interface. A second contribution consisted in a new procedure for the correction of elimination approaches in order to respect the balance of the resultant

of moments of residuals at the interface. This *a priori* moments correction allowed to significantly improve the accuracy of all the elimination approaches considered. The proposed WACA method, including this correction, seems to be a good trade-off between CPU time, implementation complexity and accuracy, especially in terms of accuracy of the stresses. Future work could focus on similar improvements of mesh tying methods for dynamic, Fluid-Structure Interaction or contact problems.

6 Appendix 1

We provide in Figure 25 the results of the convergence study, which led to the choice of the mesh density used in subsection 4.1 and thereafter as reference configurations. In both configuration the reference situation chosen for this study (n=10 and m=20) show a max displacement discretization error that is less than 2%

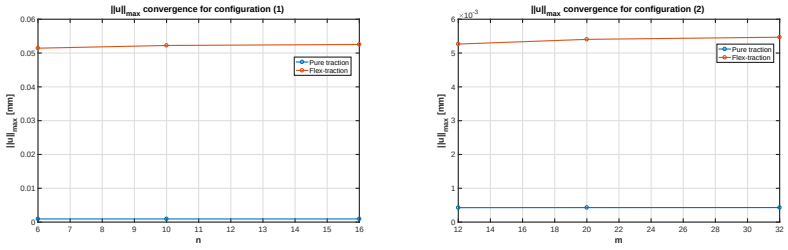

(a) (b)

Fig. 25: Convergence of the maximum displacement with mesh density : (a) for configuration (1) and (b) for configuration (2). The mesh was changed keeping the same element aspect ratio and the conforming interfaces in figure 13under the form n $\times$ n $\times$ 10 for the upper domain of configuration 1 and m $\times$ m $\times$ 10 for the upper domain of configuration 2

7 Appendix 2

In this appendix we report the detailed error analysis of each benchmark configuration, while varying the mesh density. All error measures introduced in subsection 4.2 are provided in figures 26-29 for both configuration considered.

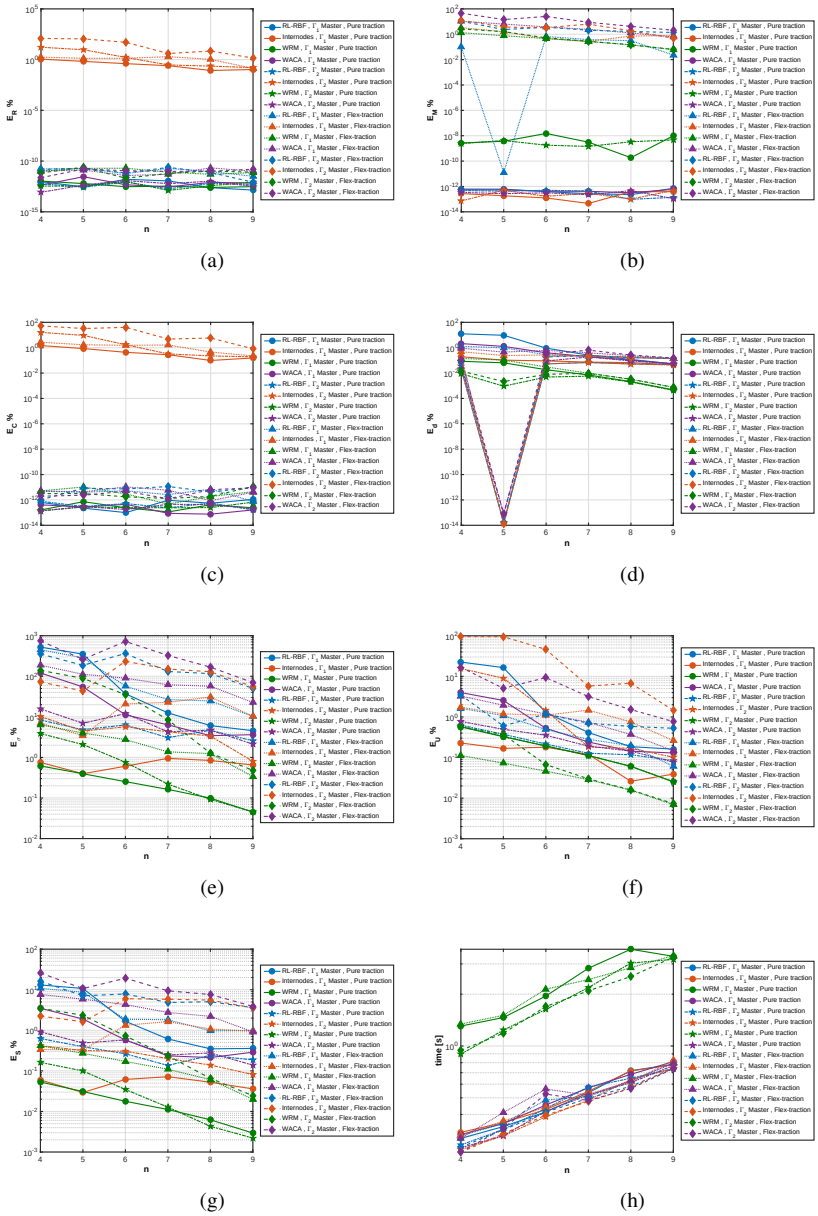

Fig. 26: Benchmark results in configuration (1) impact of n over: (a) E_R, the Resultant Force relative error, (b) E_M, the moment relative error, (c) E_c, the interface compliance relative error, (d) E_d, the displacement discontinuity relative error, (e) E_σ, the maximum of Von Mises stress relative error, (f) E_U, interface displacement field relative error, (g) E_S, average Von Mises stress relative error, (h) CPU time (s).

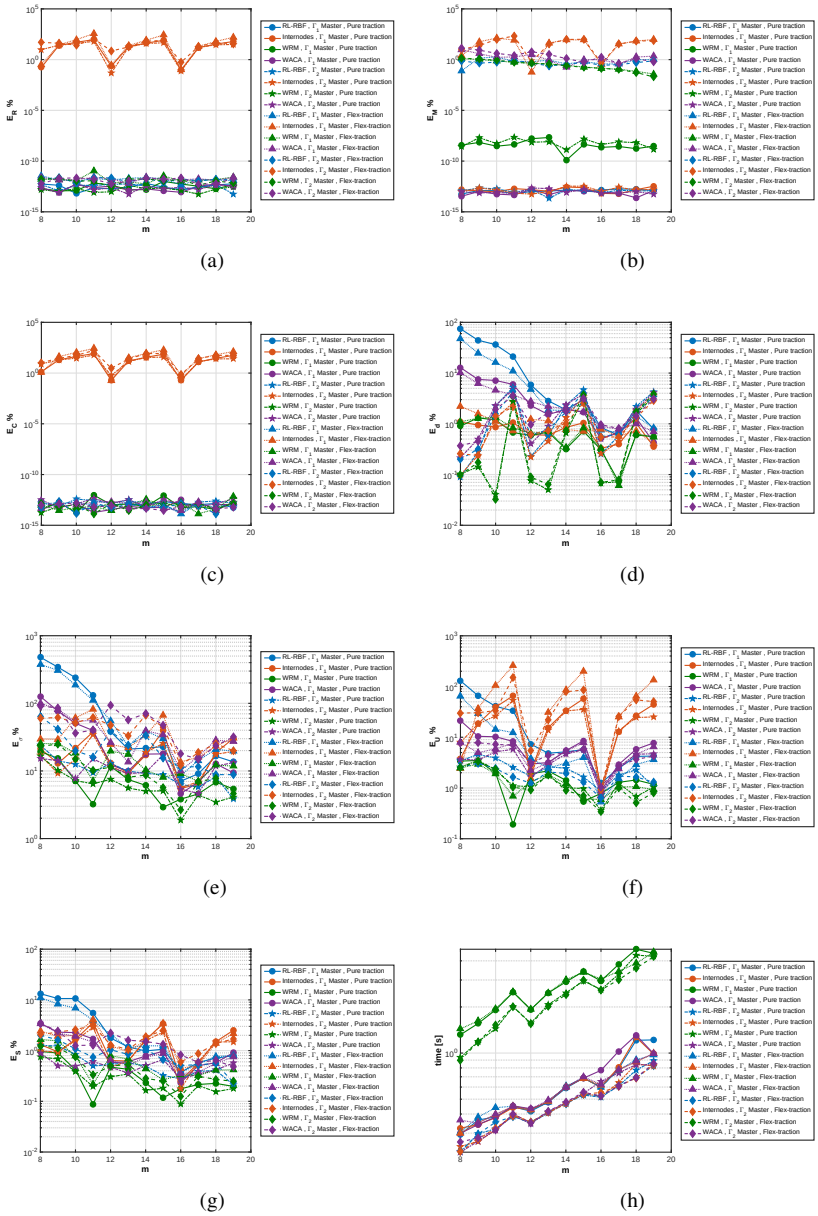

Fig. 27: Benchmark results in configuration (2)impact of m over: (a) E_R, the Resultant Force relative error, (b) E_M, the moment relative error, (c) E_c, the interface compliance relative error, (d) E_d, the displacement discontinuity relative error, (e) E_σ, the maximum of Von Mises stress relative error, (f) E_U, interface displacement field relative error, (g) E_S, average Von Mises stress relative error, (h) CPU time (s).

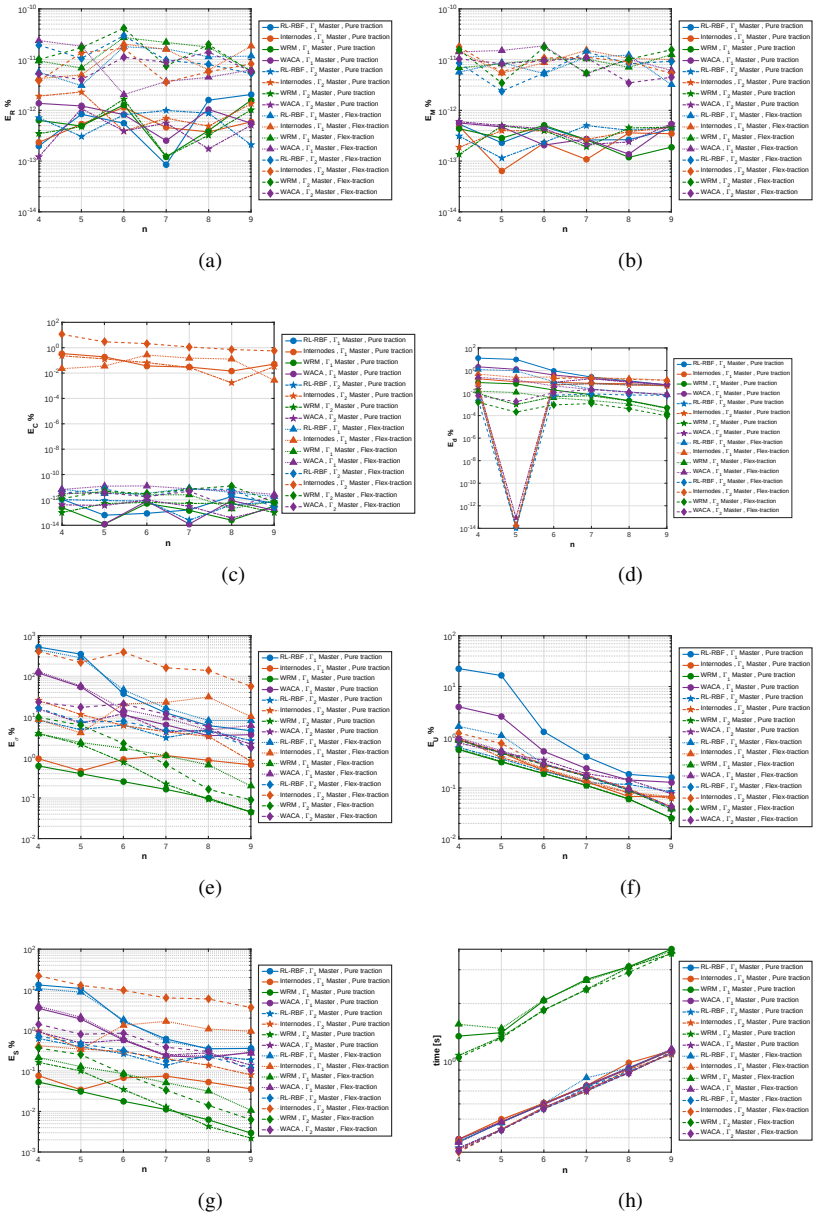

Fig. 28: Benchmark results in configuration (1) after moments balance correction. Impact of n over: (a) E_R, the Resultant Force relative error, (b) E_M, the moment relative error, (c) E_c, the interface compliance relative error, (d) E_d, the displacement discontinuity relative error, (e) E_σ, the maximum of Von Mises stress relative error, (f) E_U, interface displacement field relative error, (g) E_S, average Von Mises stress relative error, (h) CPU time (s).

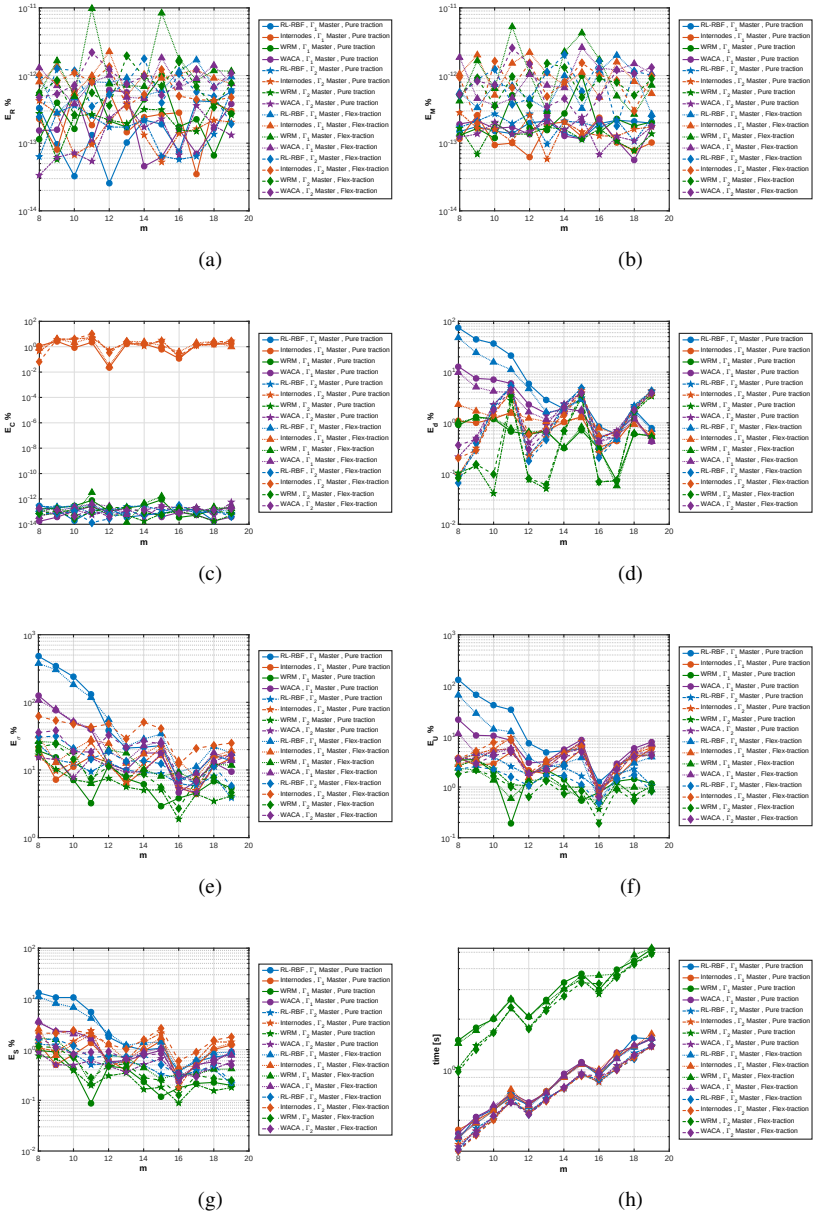

Fig. 29: Benchmark results in configuration (2) after moments balance correction. Impact of m over: (a) E_R, the Resultant Force relative error, (b) E_M, the moment relative error, (c) E_c, the interface compliance relative error, (d) E_d, the displacement discontinuity relative error, (e) E_σ, the maximum of Von Mises stress relative error, (f) E_U, interface displacement field relative error, (g) E_S, average Von Mises stress relative error, (h) CPU time (s).

8 Conflict of Interest

The authors declare that they have no conflict of interest

9 Acknowledgments

This work has been partially funded by the Association Nationale de la Recherche et de la Technologie (ANRT) through grant number CIFRE-2016/0539. We would also like to thank Dr. Simone Deparis (EPFL) for fruitful discussions, in particular with respect to the Internodes method.

References

1. Aminpour, M.A., Ransom, J.B., McCleary, S.L.: A coupled analysis method for structures with independently modelled finite element subdomains. International Journal for Numerical Methods in Engineering **38**(21), 3695–3718 (1995)
2. Babuška, I.: The finite element method with lagrangian multipliers. Numerische Mathematik **20**(3), 179–192 (1973)
3. Babuška, I., Narasimhan, R.: The babuška-brezzi condition and the patch test: an example. Computer methods in applied mechanics and engineering **140**(1-2), 183–199 (1997)
4. Barlow, J.: Constraint relationships in linear and nonlinear finite element analyses. International Journal for Numerical Methods in Engineering **18**(4), 521–533 (1982)
5. Becker, R., Hansbo, P., Stenberg, R.: A finite element method for domain decomposition with non-matching grids. ESAIM: Mathematical Modelling and Numerical Analysis **37**(2), 209–225 (2003)
6. Beckert, A., Wendland, H.: Multivariate interpolation for fluid-structure-interaction problems using radial basis functions. Aerospace Science and Technology **5**(2), 125–134 (2001)
7. Bernardi, C.: A new nonconforming approach to domain decomposition: the mortar element method. Nonlinear partial equations and their applications (1989)
8. Bernardi, C., Maday, Y., Patera, A.T.: Domain decomposition by the mortar element method. Asymptotic and numerical methods for partial differential equations with critical parameters **384**, 269–286 (1993)
9. Bertsekas, D.P.: Constrained optimization and Lagrange multiplier methods. Academic press (2014)
10. Bitencourt, L.A., Manzoli, O.L., Prazeres, P.G., Rodrigues, E.A., Bittencourt, T.N.: A coupling technique for non-matching finite element meshes. Computer Methods in Applied Mechanics and Engineering **290**, 19–44 (2015)
11. Bochev, P., Day, D.: A least-squares method for consistent mesh tying. Int. J. Num. Anal. and Modeling **4**, 342–352 (2007)
12. de Boer, A., van Zuijlen, A.H., Bijl, H.: Comparison of conservative and consistent approaches for the coupling of non-matching meshes. Computer Methods in Applied Mechanics and Engineering **197**(49), 4284–4297 (2008)
13. Brandt, A.: Multiscale scientific computation: Review 2001 pp. 3–95 (2002)
14. Buhmann, M.D.: Radial basis functions: theory and implementations, vol. 12. Cambridge university press (2003)
15. Cafiero, M., Lloberas-Valls, O., Cante, J., Oliver, J.: The domain interface method: a general-purpose non-intrusive technique for non-conforming domain decomposition problems. Computational mechanics **57**, 555 (2016)
16. CebralĪ, J.R., LČohnerē, R.: Conservative load projection and tracking for fluid-structure problems. AIAA journal **35**(4) (1997)
17. Cho, Y.S., Im, S.: Mls-based variable-node elements compatible with quadratic interpolation. part i: formulation and application for non-matching meshes. International journal for numerical methods in engineering **65**(4), 494–516 (2006)
18. Cho, Y.S., Im, S.: Mls-based variable-node elements compatible with quadratic interpolation. part ii: application for finite crack element. International Journal for Numerical Methods in Engineering **65**(4), 517–547 (2006)
19. Cho, Y.S., Jun, S., Im, S., Kim, H.G.: An improved interface element with variable nodes for non-matching finite element meshes. Computer Methods in Applied Mechanics and Engineering **194**(27), 3022–3046 (2005)

20. Christensen, P., Klarbring, A., Pang, J.S., Strömberg, N.: Formulation and comparison of algorithms for frictional contact problems. International Journal for Numerical Methods in Engineering **42**(1), 145–173 (1998)
21. D, F.J., Van, D.A.: Computer graphics principles & practice second edition in c (1996)
22. Davidon, W.: Aec research and development report. ANL-5990 (1959)
23. De Boer, A., Van Zuijlen, A., Bijl, H.: Review of coupling methods for non-matching meshes. Computer methods in applied mechanics and engineering **196**(8), 1515–1525 (2007)
24. Dennis Jr, J.E., Moré, J.J.: Quasi-newton methods, motivation and theory. SIAM review **19**(1), 46–89 (1977)
25. Dennis Jr, J.E., Schnabel, R.B.: Numerical methods for unconstrained optimization and nonlinear equations (1996)
26. Deparis, S., Forti, D., Gervasio, P., Quarteroni, A.: Internodes: an accurate interpolation-based method for coupling the galerkin solutions of pdes on subdomains featuring non-conforming interfaces. Computers & Fluids **141**, 22–41 (2016)
27. Deparis, S., Forti, D., Quarteroni, A.: A rescaled localized radial basis function interpolation on non-cartesian and nonconforming grids. SIAM Journal on Scientific Computing **36**(6), A2745–A2762 (2014)
28. Dhia, H.B., Elkhodja, N., Roux, F.X.: Multimodeling of multi-alterated structures in the arlequin framework: Solution with a domain-decomposition solver. European Journal of Computational Mechanics/Revue Européenne de Mécanique Numérique **17**(5-7), 969–980 (2008)
29. Dhia, H.B., Rateau, G.: The arlequin method as a flexible engineering design tool. International journal for numerical methods in engineering **62**(11), 1442–1462 (2005)
30. Dohrmann, C., Key, S., Heinstein, M.: A method for connecting dissimilar finite element meshes in two dimensions. International Journal for Numerical Methods in Engineering **48**(5), 655–678 (2000)
31. Dohrmann, C., Key, S., Heinstein, M.: Methods for connecting dissimilar three-dimensional finite element meshes. International Journal for Numerical Methods in Engineering **47**(5), 1057–1080 (2000)
32. Duarte, C.A., Kim, D.J.: Analysis and applications of a generalized finite element method with global–local enrichment functions. Computer Methods in Applied Mechanics and Engineering **197**(6), 487–504 (2008)
33. Duchon, J.: Splines minimizing rotation-invariant semi-norms in sobolev spaces. Constructive theory of functions of several variables pp. 85–100 (1977)
34. Duval, M., Passieux, J.C., Salaün, M., Guinard, S.: Non-intrusive coupling: recent advances and scalable nonlinear domain decomposition. Archives of Computational Methods in Engineering **23**(1), 17 (2016)
35. Farhat, C., Lesoinne, M., Le Tallec, P.: Load and motion transfer algorithms for fluid/structure interaction problems with non-matching discrete interfaces: Momentum and energy conservation, optimal discretization and application to aeroelasticity. Computer methods in applied mechanics and engineering **157**(1-2), 95–114 (1998)
36. Farhat, C., Roux, F.X.: A method of finite element tearing and interconnecting and its parallel solution algorithm. International Journal for Numerical Methods in Engineering **32**(6), 1205–1227 (1991)
37. Feyel, F., Chaboche, J.L.: Fe 2 multiscale approach for modelling the elastoviscoplastic behaviour of long fibre sic/ti composite materials. Computer methods in applied mechanics and engineering **183**(3), 309–330 (2000)
38. Fish, J., Belsky, V., Pandheeradi, M.: Iterative and direct solvers for interface problems with lagrange multipliers. Computing Systems in Engineering **6**(3), 261–273 (1995)
39. Flemisch, B., Kaltenbacher, M., Triebenbacher, S., Wohlmuth, B.: Non-matching grids for a flexible discretization in computational acoustics. Communications in Computational Physics **11**(2), 472–488 (2012)
40. Fletcher, R., Powell, M.J.: A rapidly convergent descent method for minimization. The computer journal **6**(2), 163–168 (1963)
41. Gander, M.J., Japhet, C.: Algorithm 932: Pang: software for nonmatching grid projections in 2d and 3d with linear complexity. ACM Transactions on Mathematical Software (TOMS) **40**(1), 6 (2013)
42. Gervasio, P., Quarteroni, A.: Analysis of the internodes method for non-conforming discretizations of elliptic equations (2016)
43. Hartmann, S., Oliver, J., Weyler, R., Cante, J., Hernández, J.: A contact domain method for large deformation frictional contact problems. part 2: Numerical aspects. Computer Methods in Applied Mechanics and Engineering **198**(33), 2607–2631 (2009)
44. Heintz, P., Hansbo, P.: Stabilized lagrange multiplier methods for bilateral elastic contact with friction. Computer methods in applied mechanics and engineering **195**(33), 4323–4333 (2006)
45. Hinton, E., Campbell, J.: Local and global smoothing of discontinuous finite element functions using a least squares method. International Journal for Numerical Methods in Engineering **8**(3), 461–480 (1974)
46. Hou, G., Wang, J., Layton, A.: Numerical methods for fluid-structure interaction - a review. Communications in Computational Physics **12**(2), 337–377 (2012)

47. Jeong, G.E., Youn, S.K., Park, K.: Element-independent implementation for method of lagrange multipliers. World Academy of Science, Engineering and Technology, International Journal of Mechanical, Aerospace, Industrial, Mechatronic and Manufacturing Engineering **11**(2), 343–347 (2017)
48. Kim, H.G.: Interface element method: Treatment of non-matching nodes at the ends of interfaces between partitioned domains. Computer methods in applied mechanics and engineering **192**(15), 1841–1858 (2003)
49. Lim, J.H., Im, S., Cho, Y.S.: Mls (moving least square)-based finite elements for three-dimensional nonmatching meshes and adaptive mesh refinement. Computer methods in applied mechanics and engineering **196**(17), 2216–2228 (2007)
50. Lim, J.H., Im, S., Cho, Y.S.: Variable-node elements for non-matching meshes by means of mls (moving least-square) scheme. International Journal for Numerical Methods in Engineering **72**(7), 835–857 (2007)
51. Lloberas-Valls, O., Cafiero, M., Cante, J., Ferrer, A., Oliver, J.: The domain interface method in non-conforming domain decomposition multifield problems. Computational Mechanics **59**(4), 579–610 (2017)
52. Lloberas-Valls, O., Rixen, D., Simone, A., Sluys, L.: Multiscale domain decomposition analysis of quasi-brittle heterogeneous materials. International Journal for Numerical Methods in Engineering **89**(11), 1337–1366 (2012)
53. Lloberas-Valls, O., Rixen, D., Simone, A., Sluys, L.: On micro-to-macro connections in domain decomposition multiscale methods. Computer Methods in Applied Mechanics and Engineering **225**, 177–196 (2012)
54. Löhner, R., Yang, C., Cebral, J., Baum, J.D., Luo, H., Pelessone, D., Charman, C.: Fluid-structure-thermal interaction using a loose coupling algorithm and adaptive unstructured grids. In: Proc., 29th AIAA Fluid Dynamics Conference (1998)
55. Mandel, J.: Balancing domain decomposition. International Journal for Numerical Methods in Biomedical Engineering **9**(3), 233–241 (1993)
56. McGee, W., Seshaiyer, P.: Non-conforming finite element methods for nonmatching grids in three dimensions. Domain decomposition methods in science and engineering pp. 327–334 (2005)
57. Nitsche, J.: Über ein variationsprinzip zur lösung von dirichlet-problemen bei verwendung von teilräumen, die keinen randbedingungen unterworfen sind **36**(1), 9–15 (1971)
58. Oliver, J., Hartmann, S., Cante, J., Weyler, R., Hernández, J.: A contact domain method for large deformation frictional contact problems. part 1: theoretical basis. Computer Methods in Applied Mechanics and Engineering **198**(33), 2591–2606 (2009)
59. Park, K., Felippa, C., Rebel, G.: A simple algorithm for localized construction of non-matching structural interfaces. International Journal for Numerical Methods in Engineering **53**(9), 2117–2142 (2002)
60. Puso, M.A.: A 3d mortar method for solid mechanics. International Journal for Numerical Methods in Engineering **59**(3), 315–336 (2004)
61. Puso, M.A., Laursen, T.A.: A mortar segment-to-segment contact method for large deformation solid mechanics. Computer methods in applied mechanics and engineering **193**(6), 601–629 (2004)
62. Quiroz, L., Beckers, P.: Non-conforming mesh gluing in the finite elements method. International Journal for Numerical Methods in Engineering **38**(13), 2165–2184 (1995)
63. Rixen, D.J.: Substructuring and dual methods in structural analysis. Ph.D. thesis (1997)
64. Shi, Z.C.: The fem test for convergence of nonconforming finite elements. Mathematics of computation **49**(180), 391–405 (1987)
65. Shillor, M., Sofonea, M., Telega, J.J.: 7 elastic contact. In: Models and Analysis of Quasistatic Contact, pp. 101–115. Springer (2004)
66. Smith, M.J., Cesnik, C.E., Hodges, D.H.: Evaluation of some data transfer algorithms for noncontiguous meshes. Journal of Aerospace Engineering **13**(2), 52–58 (2000)
67. Sofonea, M., Han, W., Shillor, M.: Analysis and approximation of contact problems with adhesion or damage. CRC Press (2005)
68. Song, Y.U., Youn, S.K., Park, K.: Virtual gap element approach for the treatment of non-matching interface using three-dimensional solid elements. Computational Mechanics pp. 1–10 (2017)
69. Stummel, F.: The generalized patch test. SIAM Journal on Numerical Analysis **16**(3), 449–471 (1979)
70. Stummel, F.: The limitations of the patch test. International journal for numerical methods in engineering **15**(2), 177–188 (1980)
71. Thévenaz, P., Blu, T., Unser, M.: Interpolation revisited [medical images application]. IEEE Transactions on medical imaging **19**(7), 739–758 (2000)
72. Tian, R., Yagawa, G.: Non-matching mesh gluing by meshless interpolationan alternative to lagrange multipliers. International journal for numerical methods in engineering **71**(4), 473–503 (2007)
73. Wang, X., Prakash, A., Chen, J.S., Taciroglu, E.: Variationally consistent coupling of non-matching discretizations for large deformation problems. Computational Mechanics (2017)

74. Wendland, H.: Piecewise polynomial, positive definite and compactly supported radial functions of minimal degree. Advances in computational Mathematics **4**(1), 389–396 (1995)
75. Wriggers, P.: Finite element algorithms for contact problems. Archives of Computational Methods in Engineering **2**(4), 1–49 (1995)